| | |
|---|---|
| **Titre:** Title: | Topology Optimization of a Blended Wing Body Aircraft : An Interpretable Structural Design |
| **Auteur:** Author: | Mehdi Djitli |
| **Date:** | 2025 |
| **Type:** | Mémoire ou thèse / Dissertation or Thesis |
| **Référence:** Citation: | Djitli, M. (2025). Topology Optimization of a Blended Wing Body Aircraft : An Interpretable Structural Design [Mémoire de maîtrise, Polytechnique Montréal]. PolyPublie. https://publications.polymtl.ca/68485/ |



| | |
|---|---|
| **URL de PolyPublie:** PolyPublie URL: | https://publications.polymtl.ca/68485/ |
| **Directeurs de recherche:** Advisors: | Sofiane Achiche, & Aurelian Vadean |
| **Programme:** Program: | Génie mécanique |

**POLYTECHNIQUE MONTRÉAL**
affiliée à l'Université de Montréal

# Topology Optimization of a Blended Wing Body Aircraft : An Interpretable Structural Design

**MEHDI DJITLI**
Département de génie mécanique

Mémoire présenté en vue de l'obtention du diplôme de *Maîtrise ès sciences appliquées*
Génie mécanique

Août 2025

**POLYTECHNIQUE MONTRÉAL**
affiliée à l'Université de Montréal

Ce mémoire intitulé :

**Topology Optimization of a Blended Wing Body Aircraft : An Interpretable Structural Design**

présenté par **Mehdi DJITLI**
en vue de l'obtention du diplôme de *Maîtrise ès sciences appliquées*
a été dûment accepté par le jury d'examen constitué de :

**Louis LABERGE LEBEL**, président
**Sofiane ACHICHE**, membre et directeur de recherche
**Aurelian VADEAN**, membre et codirecteur de recherche
**Nicolas DODANE**, membre

## DEDICATION

*I dedicate this thesis to my future self,*
*who will look back on this distinct period of my life,*
*a time that has crystallized and will continue to shape me . . .*

*One can choose to go back toward safety or forward toward growth.*
*Growth must be chosen again and again.*
*Fear must be overcome again and again.*
*- Abraham Maslow*

# ACKNOWLEDGEMENTS

I would first like to thank Professor Sofiane Achiche for his support and supervision throughout the project. He greatly helped me navigate the uncertainties of a research project. I would also like to thank Professor Aurelian Vadean, who also supervised me and contributed with his expertise in structural design. Both Sofiane and Aurelian taught me how to apply scientific rigor in my work.

A special thanks to Tom Raffy, an exceptional intern at the lab, whose expertise and knowledge in aircraft structures greatly accelerated the project. With his help, we made rapid progress and learned a lot together. I especially appreciate that you taught me how to create outstanding artwork for multiple figures in this thesis. It has been an honor to work with you over these four months.

I would also like to thank everyone who was at the lab during my time here. We shared many great conversations and laughs over fascinating topics. I will always remember the determination not to lose at Uno: Show them no mercy, just to avoid the infernal spicy sauce!

A heartfelt thank you to everyone close to me who supported me throughout my master's. You are the ones who made this possible.

Finally, I extend my gratitude to the Fondation Arbour, Hydro-Québec and the Natural Sciences and Engineering Research Council of Canada for their financial support. These three prestigious scholarships allowed me to focus my efforts on both my research and my well-being.

I would like to acknowledge the assistance of ChatGPT for helping refine the formulation of certain sections of this thesis. All intellectual contributions, analyses, and conclusions remain my own.

# RÉSUMÉ

L'avion à fuselage intégré (BWB) représente une innovation majeure dans le domaine de l'aéronautique, offrant un potentiel considérable pour la réduction des émissions de gaz à effet de serre et l'amélioration de l'efficacité aérodynamique. Toutefois, sa géométrie non conventionnelle entraîne des défis structurels spécifiques, notamment en ce qui concerne l'identification des trajectoires de raidissement optimales et la distribution des raidisseurs. Cette thèse aborde ces enjeux en développant un cadre d'optimisation topologique (OT) adapté à la conception structurelle, avec un accent particulier sur l'interprétabilité et la rigidité des résultats.

L'étude débute par la proposition d'une nouvelle métrique de performance pour évaluer les résultats de l'OT basée sur la densité, qui combine des mesures de rigidité structurelle et d'interprétabilité. Cette métrique est validée par son application à un modèle de poutre en porte-à-faux, illustrant son efficacité dans l'orientation des décisions de conception en phase préliminaire. Le cadre est ensuite étendu à l'avion BWB pour optimiser une structure de coque raidis. Les chargements analysés sont : la flexion verticale des ailes, l'atterrissage dynamique, le roulis et la poussée des moteurs.

Les résultats principaux révèlent des trajectoires de raidissement distinctes. La coque raidie exploite la double courbure pour maximiser la rigidité à l'aide de membrures fines intégrées. La superposition des topologies optimisées pour la coque raidie à l'aide d'algorithmes de traitement d'images met en évidence des motifs structurels récurrents, soulignant les régions critiques qui nécessitent un renforcement. Ces résultats démontrent le potentiel de l'optimisation topologique pour concevoir des BWB légers et performants tout en équilibrant les contraintes de performance.

Nous avons ensuite fabriqué la structure de la coque raidie du BWB à l'aide d'une imprimante 3D à filament pour le cas de charge de flexion verticale des ailes, en intégrant la topologie optimale obtenue par notre méthode à la peau aérodynamique, afin de créer une version miniature d'un BWB optimisé ayant comme but de démontrer la faisabilité de la fabrication d'une coque raidie complexe issue de résultats d'OT.

Cette recherche présente une méthodologie systématique permettant d'intégrer l'OT dans la conception préliminaire en aérospatiale, ouvrant ainsi la voie à de futures avancées dans le développement des BWB et de l'aviation durable.

# ABSTRACT

The blended wing body (BWB) aircraft represents a major innovation in aeronautics, offering significant potential for reducing greenhouse gas emissions and improving aerodynamic efficiency. However, its unconventional geometry introduces specific structural challenges, particularly regarding the identification of optimal stiffening trajectories and the distribution of stiffeners. This thesis addresses these challenges by developing a topology optimization (TO) framework tailored to structural design, with a particular focus on result interpretability and stiffness.

The study begins with the introduction of a novel performance metric for evaluating TO results based on density distribution. This metric combines structural stiffness and interpretability measurements. It is validated through its application to a cantilever beam model, demonstrating its effectiveness in guiding early design decisions. The framework is then extended to the BWB aircraft, using a stiffened shell structure, and analyzed in critical loading cases, including vertical wing upbending, dynamic landing, roll, and engine thrust.

The main results reveal distinct stiffening trajectories. The stiffened shell leverages double curvature to maximize rigidity through integrated fine stiffeners. The superposition of optimized topologies for the stiffened shell highlights recurring structural patterns, identifying critical regions that require reinforcement. These findings demonstrate the potential of TO in designing lightweight and high-performance BWB aircraft while balancing performance constraints.

Next, we manufactured the stiffened shell structure of the BWB for the upbending load case, showcasing how the optimal topology obtained from our approach can be incorporated with the aerodynamic skin to produce a scaled version of a real-world optimized BWB to demonstrate the feasibility of the manufactured of a stiffened shell derived from topology optimization results.

This research presents a systematic methodology for integrating TO into preliminary aerospace design, paving the way for future advancements in BWB development and sustainable aviation.

# TABLE OF CONTENTS

# LIST OF TABLES

# LIST OF FIGURES

# LIST OF SYMBOLS AND ACRONYMS

| | |
|---|---|
| BWB | Blended Wing Body |
| DOF | Degree of freedom |
| DP | Discreteness Parameter |
| DI | Discreteness Index |
| FEA | Finite Element Analysis |
| FEM | Finite Element Model |
| MINDIM | Minimum size member |
| MAXDIM | Maximum size member |
| NASA | National Aeronautics and Space Administration |
| PLA | Polylactic acid |
| PLOAD4 | Pressure Load Type 4 |
| SAF | Sustainable aviation fuel |
| SIMP | Solid Isotropic Material with Penalization |
| RBE3 | Rigid Body Element Type 3 |
| TAW | Tube and Wing |
| TO | Topology Optimization |

| | |
|---|---|
| $C$ | Compliance |
| $E$ | Young's modulus |
| $\mathbf{F}$ | Force vector |
| $I$ | Moment of inertia |
| $\mathbf{K}(\rho)$ | Global stiffness matrix dependent on the material distribution |
| $P_{cr}$ | Critical buckling load |
| $V(\rho)$ | Volume fraction of the design space |
| $\mathbf{u}$ | Displacement vector |
| $\rho$ | Density |
| $\rho_e$ | Density of an element |
| $\sigma_{ult}$ | Ultimate tensile strength |
| $\sigma_y$ | Yield Strength |

# CHAPTER 1 INTRODUCTION

## 1.1 The Rationale for Developing the Blended Wing Body Aircraft

Blended Wing Body (BWB) aircraft are a new paradigm in aeronautics, with the potential to reduce greenhouse gases by 27% compared with conventional aircraft [1]. Its design significantly deviates from conventional aircraft, often referred to in the literature as "The Aerodynamic Renaissance". The concept is based on continuity between the wings and the fuselage, to reduce the wetted surface and improve the lift/thrust ratio. These advantages derive from the integration of a lift-generating center, combined with conventional outer wings [1]. For the same passenger or cargo requirements, this design means a shorter aircraft relative to the roll axis than traditionally obtained with tubes and wing (TAW). Figure 1.1a shows NASA's research project on integrated fuselage aircraft, with the X-48B prototype [2] and Figure 1.1b shows JetZero commercial project on integrated fuselage aircraft, with the Z4 BWB Concept.


(a) X48B developped by NASA

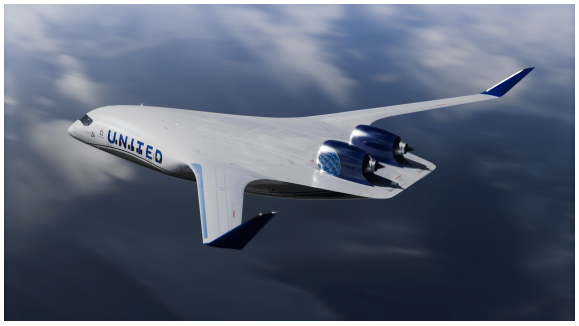


(b) Z4 developped by JetZero

Figure 1.1 NASA and JetZero BWB Concept [3] [4]

The industry seems to be moving towards this type of aircraft for a variety of reasons, that include fuel economy, reduced structural weight and noise reduction [5]. It could be the next step in efficiency due to the structural benefits potentially coupled with sustainable aviation fuel (SAF) engines to reach the net zero emission by 2050 set by the International Air Transport Association in 2021 [6].

Figure 1.2 shows the lift and weight distribution along the wingspan of both a TAW and BWB aircraft. We can see a continuous lift on the flying wing compared to the tubular fuselage with wings, due to the cylindrical shape of the fuselage. There is also an inertial concentration at the cylindrical fuselage level since for obvious reasons the aircraft's structural and functional

mass is located at the tube level. The weight of the BWB is more evenly distributed along the pitch axis, because of the rectangular shape of the aircraft's functional area.

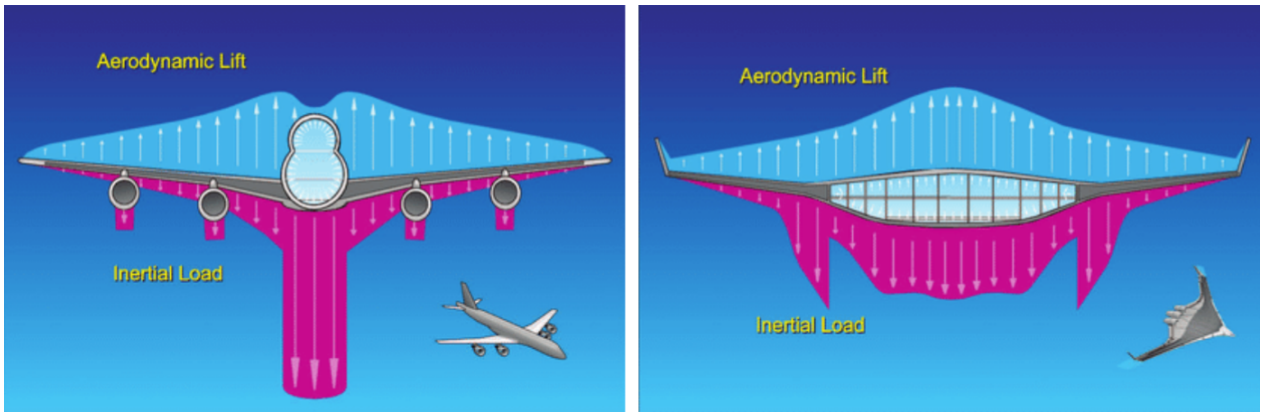


Figure 1.2 Comparison of Aerodynamic Lift and Inertial Load Distribution Along the Wingspan of TAW and BWB Aircraft [7]

## 1.2 Challenges of the Blended Wing Body aircraft

The BWB aircraft has some interesting features to reduce carbon emissions of the plane and make the aviation industry greener. This new promising design comes with multiple challenges that need to be solved before a commercial plane is available. These main challenges are stability and control, current airport infrastructure, and structural design [8].

### 1.2.1 Stability and Control Surfaces

Unlike TAW aircraft, BWB aircraft configuration tends to have rear engines for aerodynamics and sound preferences. The BWB has also no horizontal stabilizer like the TAW which can lead to less stability of the BWB aircraft [9]. Thanks to fly-by-wire technology already integrated into the TAW design, along with active control surfaces, it remains possible to actively stabilize the aircraft [9]. In Figure 1.3, we can see a possible configuration of control surfaces of a BWB aircraft.

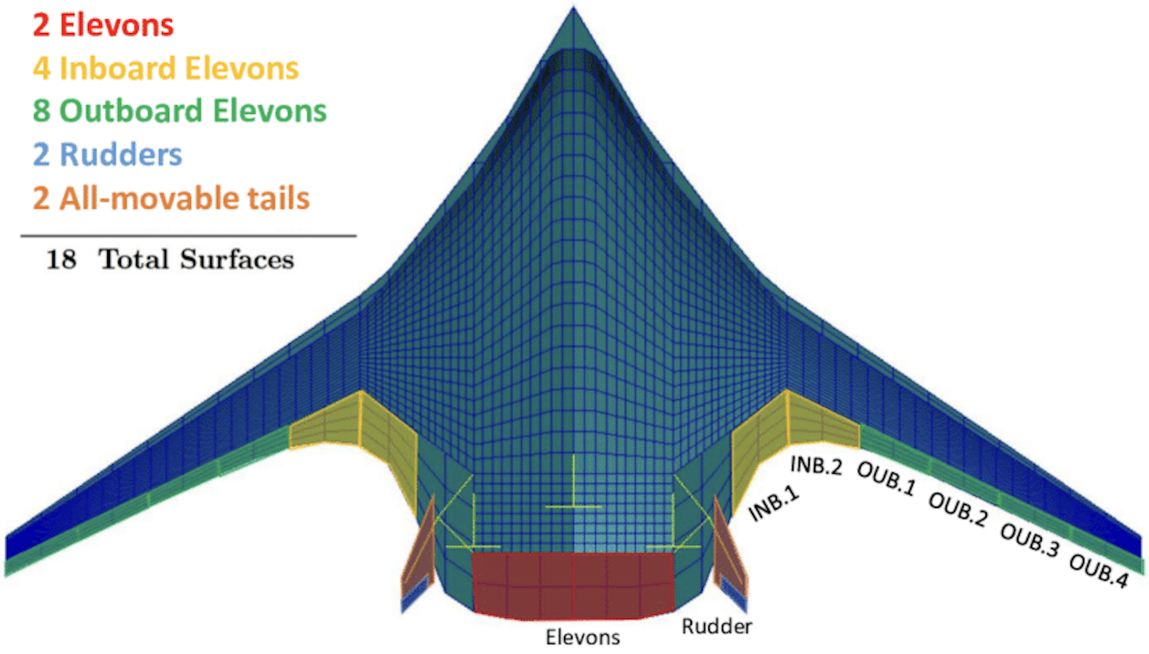


Figure 1.3 Illustration of the control surface configuration and structural layout of a BWB aircraft, featuring two elevons, four inboard elevons, eight outboard elevons, two Rudders, and two all-movable tails [10]

In this configuration, the 18 control surfaces provide sufficient capability to actively stabilize and control the BWB aircraft in flight, allowing for precise adjustments to yaw, pitch, and roll. The two V-shaped rudders primarily influence Yaw. Roll adjustments are mainly achieved through the eight outboard elevons, while pitch adjustments are predominantly managed by the two inboard elevons. Additionally, the inboard elevons are versatile, contributing to the modulation of all three Euler angles, depending on the flight conditions [10]. With these active control surfaces and fly-by-wire technology, the BWB would still gets inferior flying and handling qualities than TAW because of the lack of a passive horizontal stabilizer [8].

### 1.2.2 Airport Infrastructure

BWB aircraft, with their wider wingspans compared to conventional planes of the same passenger capacity, face several integration challenges with existing airport infrastructure. Their larger size complicates accommodation at current gates and terminals, as these are designed for the narrower wingspans of traditional aircraft, potentially reducing the number of aircraft that can dock simultaneously [11]. Their increased overall size and uniform weight distribution across the wing likely require larger and more widely spaced landing gear. This, in turn, may require larger runways at airports to accommodate them. We can see the

difference in size between the Boeing-Nasa BWB design and the Boeing 747-400 in Figure 1.4

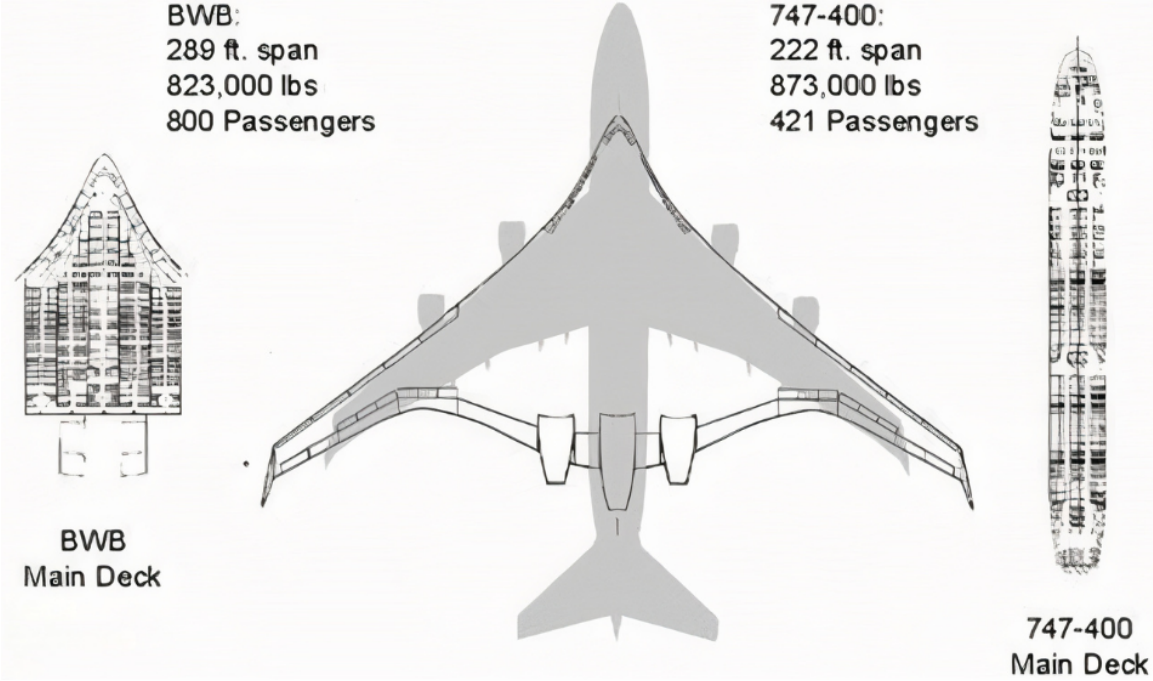


Figure 1.4 Comparison of wingspan and fuselage length between the Boeing BWB and the Boeing 747-400. The BWB's higher aspect ratio enables it to accommodate nearly double the number of passengers compared to the 747-400 [12]

The distinct shape of the BWB may require redesigned boarding bridges and ground support equipment for alignment and efficient servicing. In addition, their unique internal layouts could complicate emergency evacuations, particularly for passengers seated outside the aisles. Furthermore, BWB aircraft face aerodynamic challenges at lower speeds, particularly during take-off and landing, requiring careful management to ensure safety and stability in an airport [10].

### 1.2.3 Structural Design and Manufacturing

The structural design and manufacturing of BWB aircraft present significant challenges, primarily due to their double curvature shape. One drawback of the BWB design is that its non-cylindrical shape is less effective at handling internal pressurization compared to a traditional cylindrical fuselage. A cylindrical fuselage is optimal for managing internal pressure because the stress on the membrane increases linearly with the geometrical ratio $R/t$ where $R$ is the radius of the pressure shell and $t$ is its thickness. In comparison, a rectangular geometry is subject to non-linear stresses, as illustrated by the shell deformation

in Figure 1.5.

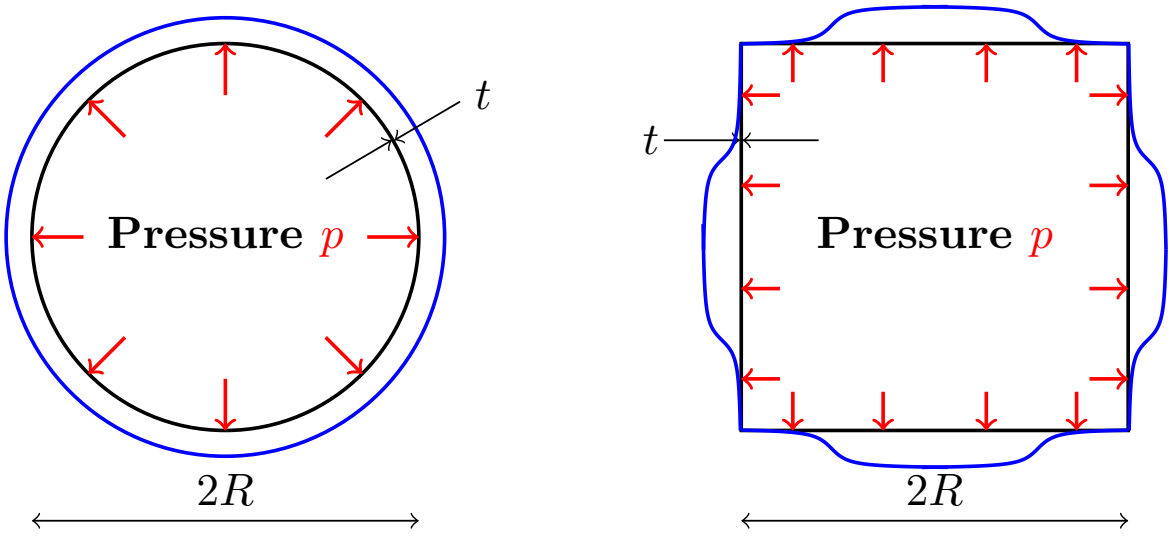


Figure 1.5 Deformation of the Pressure Shell (shown in blue) for a Cylindrical Shell with Radius $R$, Thickness $t$, and a Rectangular Shape of Length $2R$

In rectangular pressure vessels, membrane stress exhibits a quadratic increase with the geometric ratio due to bending effects. This presents a design challenge for aircraft structures with elliptical geometries, intermediate between rectangular and cylindrical shapes, such as BWB configurations. Additionally, the double-curvature rectangular shape of the BWB presents unique challenges from a design and manufacturing point of view, resulting in an optimal structural configuration that could differs significantly from conventional TAW aircraft. A traditional orthogrid configuration, commonly used on TAWs, would be challenging to assemble and scale on a BWB aircraft due to the continuously varying curvature at the wing-fuselage junction. However, advancements in composite materials, additive manufacturing and innovative structural optimization techniques provide effective solutions to these challenges, facilitating the development of strong yet lightweight BWB aircraft. These topics will be discussed in more detail in Chapter 2.

# CHAPTER 2 LITERATURE REVIEW

## 2.1 Typical Aircraft Structural Design

This section explores the design of a typical aircraft, focusing on its structural architecture. We will first examine the two most common structural configurations: monocoque and semi-monocoque. Following this, we will cover the materials commonly used in aircraft construction, highlighting their role in ensuring optimal strength, weight, and performance. Additionally, we will discuss the design of the primary structural components, specifically the fuselage and wings.

### 2.1.1 Aircraft Structural Architectures

#### Monocoque Architecture

A monocoque structure relies on the external skin of the aircraft to bear the primary structural loads, as suggested by its name, meaning "single-shell". To maintain the shape of the structure under pressurization, formers are used, while bulkheads act as structural walls to separate pressurized and non-pressurized sections of the aircraft, as illustrated in Figure 2.1.

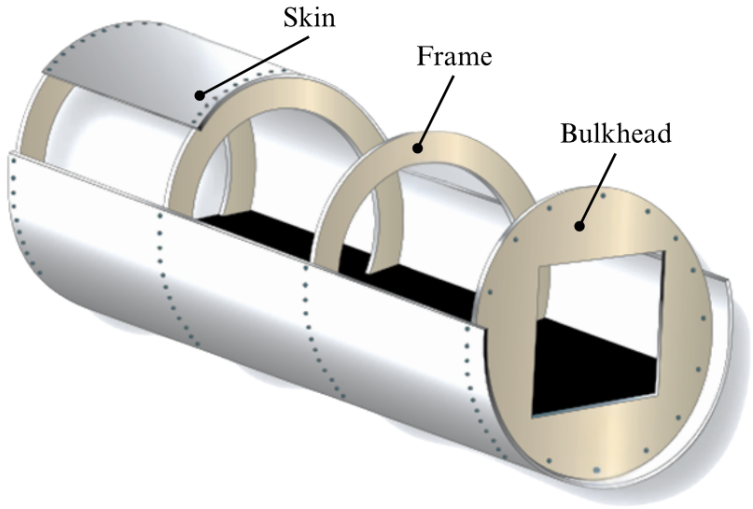


Figure 2.1 Typical monocoque aircraft structure showing the structural skin, formers, and bulkhead components. Adapted from [13]

Although monocoque structures are simpler to manufacture compared to semi-monocoque structures, they are not optimal in terms of strength-to-weight ratio. A thick skin is re-

quired to provide sufficient structural integrity, which increases weight without significantly improving load distribution efficiency.

### Semi-Monocoque Architecture

The semi-monocoque structure was developed to reduce weight while maintaining structural integrity. It follows the same fundamental principle as the monocoque design but replaces the thick external skin with a thinner, lighter skin reinforced by internal structural elements such as stringers and longerons, as illustrated in Figure 2.2.

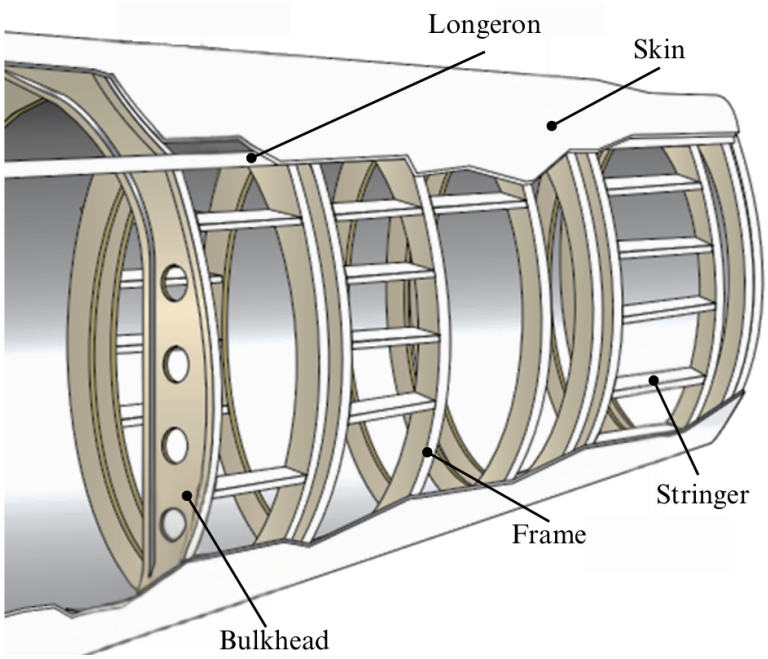


Figure 2.2 Typical semi-monocoque aircraft architecture showing the aerodynamic skin, longerons, stringers, and bulkhead components. Adapted From [13]

This design achieves a better strength-to-weight ratio, making it more fuel-efficient and widely adopted in modern aircraft. However, a key challenge of semi-monocoque structures is buckling. As the external skin becomes thinner to reduce weight, it becomes more susceptible to compressive loads, which can cause local or global buckling, potentially compromising structural integrity.

The use of stiffeners in the structure help prevent buckling by reinforcing the skin. A panel in compression with the same cross section area will behave differently based on the geometry as seen in Figure 2.3. Panel (a) fails completely under the compression load, resulting in global buckling, whereas panels (b) and (c) are able to withstand the compression load due

to the bending shape or the addition of a stiffener, enhancing the compression stiffness with out of plane features.

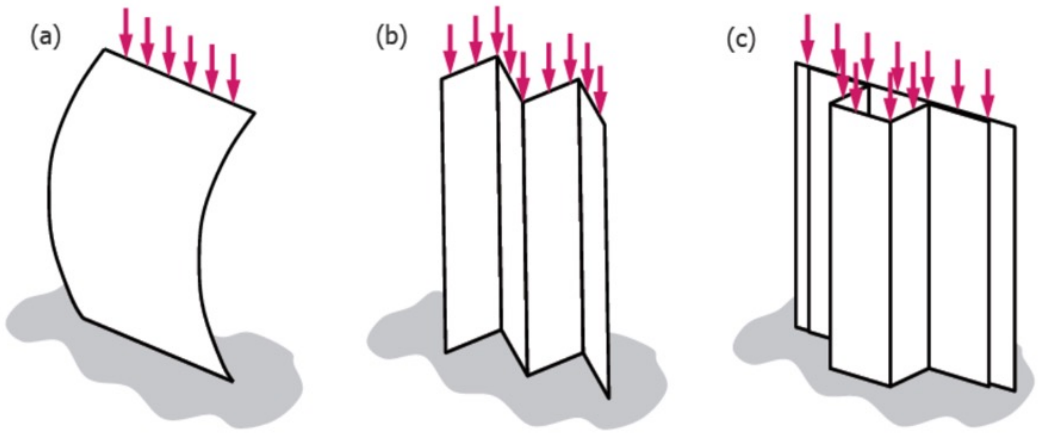


Figure 2.3 Deformation of Different Sheet Shapes Under Compression: (a) Flat Sheet, (b) Bent Sheet, and (c) Sheet with Hat Stiffener. [14]

This phenomenon can be explained using the Euler Buckling Equation:

$$P_{cr} = \frac{n\pi^2 EI}{L^2} \tag{2.1}$$

where $P_{cr}$ is the critical buckling load, $n$ is a factor that depends on the end boundary conditions, $E$ is the Young's Modulus of the sheet material, $I$ is the moment of inertia of the sheet in the direction of the applied load, and $L$ is the length of the sheet material along the direction of the applied load.

The moment of inertia $I$ for a sheet in its thickness direction is given by:

$$I = \frac{bt^3}{12} \tag{2.2}$$

Where $b$ represents the panel's width and $t$ its thickness. Adding stiffeners to a thin sheet increases its moment of inertia by affecting the lateral dimension $t$, which has a cubic influence on the moment of inertia.

$$P_{cr} \propto I \propto t^3$$

This improvement increases the force required to initiate buckling in thin skin panels in a cubic manner, while the added weight increases linearly, resulting in a significant boost to the stiffness-to-weight ratio. This is one of the reasons why reinforced skin with stiffeners is currently used in the aerospace industry.

### 2.1.2 Advanced Materials Used in Aircraft Structures

#### Metals Used in Aircraft Structures

Throughout history, metals have been primarily utilized because of their manufacturing capabilities, cost-effectiveness, and scalability in production. Table 2.1 presents the typical mechanical properties of various metals and their alloys used in aircraft structures, specifically focusing on their Young's modulus ($E$), yield strength ($\sigma_y$), ultimate tensile strength ($\sigma_{ult}$), and density ($\rho$).

Table 2.1 Typical Mechanical properties of metals and their alloys [15]

| **Metal** | **Alloy** | **E** [GPa] | $\boldsymbol{\sigma_y}$ [MPa] | $\boldsymbol{\sigma_{ult}}$ [MPa] | $\boldsymbol{\rho}$ [g/cm$^3$] |
|---|---|---|---|---|---|
| Steel | AISI 301 | 193 | 965 | 1257 | 8.00 |
| | AISI 4340 | 205 | 470 | 745 | 7.85 |
| | D6AC | 210 | 1724 | 1931 | 7.87 |
| Aluminum | AA 2024-T3 | 72 | 345 | 483 | 2.78 |
| | AA 7475-T761 | 70 | 448 | 517 | 2.81 |
| Titanium | Ti6Al-4V | 114 | 880 | 950 | 4.43 |
| Magnesium | AZ31B-H24 | 45 | 221 | 290 | 1.78 |

In the design of aircraft structures, material selection is a critical process requiring a balance between high strength and low weight. Additionally, manufacturing constraints and fatigue performance must be carefully considered. The following observations summarize these key aspects:

- **Steel Alloys:** Alloys such as AISI 301, AISI 4340, and D6AC exhibit high values of $E$, $\sigma_y$, and $\sigma_{ult}$, indicating excellent stiffness and strength. They also demonstrate good fatigue resistance, making them suitable for highly loaded structural components subjected to cyclic stresses. However, their high density limits their use in weight-sensitive aerospace applications. Additionally, steel alloys typically require complex machining and heat treatment processes, which can increase manufacturing cost and time.

- **Aluminum Alloys:** Alloys like AA 2024-T3 and AA 7475-T761 are widely used in aerospace structures due to their favorable balance of moderate strength and low density. While their Young's modulus is lower than that of steel, the associated weight savings are significant. Aluminum alloys also offer good fatigue performance, particularly when treated and assembled properly. From a manufacturing perspective, they are relatively easy to machine and form, making them cost-effective choices for large-scale production.

- **Titanium Alloy:** Ti6Al-4V provides a compelling combination of high strength, corrosion resistance, and relatively low density compared to steel. It also offers excellent fatigue resistance, especially under high-cycle conditions. However, titanium is notoriously difficult to machine due to its low thermal conductivity and tendency to gall, which increases manufacturing complexity and cost. Despite this, it remains a preferred material for critical load-bearing aerospace components.

- **Magnesium Alloy:** AZ31B-H24 has the lowest density among the materials listed, making it highly attractive for weight-critical applications. However, its lower strength and stiffness limit its use to less structurally demanding components. Magnesium alloys generally have lower fatigue strength and require careful design to avoid stress concentrations. From a manufacturing standpoint, they offer good machinability but pose challenges related to flammability during processing and corrosion susceptibility.

### Composites Used in Aircraft Structures

Advancements in composites manufacturability have led to significant weight savings in the aviation industry. Modern aircraft such as the Boeing 787 and Airbus A350 consist of approximately 50 percent composites by mass and nearly 80 percent by volume [16]. Composites can be formed into complex shapes, providing aerodynamic benefits. The most common composite used in aircraft structures is carbon fiber-reinforced polymer (CFRP). The fibers can be oriented in multiple directions inside the matrix to tailor mechanical properties according to the load type.

It is easier to select a material for a specific application based on its performance index rather than just its raw properties. Table 2.2 provides a clearer understanding of the tensile and compressive stiffness of materials while minimizing weight.

Table 2.2 Typical specific material properties used in aircraft structures [15]

| **Material** | $\boldsymbol{E/\rho}$ $[MN\,m\,kg^{-1}]$ | $\frac{\sqrt[3]{E}}{\rho}$ $[m^{7/3}N^{1/3}kg^{-1}]$ |
|---|---|---|
| AA 2024-T3 | 25.90 | 1.50 |
| AA 7475-T761 | 24.91 | 1.47 |
| AISI 4340 | 26.10 | 0.75 |
| Ti6Al-4V | 25.70 | 1.09 |
| Isotropic carbon composite | 32.70 | 2.45 |
| Isotropic E-glass fibre composite | 5.26 | 1.09 |

One of the use of this table is to see that a material that provides the highest stiffness-to-weight ratio in tension may not necessarily do so in compression, as seen in the case of AISI 4340 compared with Ti-6Al-4V.

For metals, it is obvious that aluminum alloys AA2024-T3 and AA7475-T761 are well suited for aircraft structures due to their high stiffness-to-weight ratio in both tension and compression compared to steel. However, isotropic carbon composites are an even better choice than aluminum, as they achieve the highest scores in both types of loading. The mechanical properties of CFRP in the structure are highly influenced by the manufacturing process used. However, its advantages over aluminum in recent years are evident.

### 2.1.3 Design of Main Aircraft Components

#### Fuselage Design

The fuselage is primarily viewed as a functional structure designed to carry passengers or cargo. However, it also plays a critical role in withstanding various loads, such as aerodynamic forces generated when the aircraft maneuvers through the air. The distribution of mass within the fuselage also induces bending, while internal pressurization is necessary to maintain cabin pressure at high altitudes. Figure 2.4 illustrates the typical internal skeletal framework that supports the aerodynamic skin.

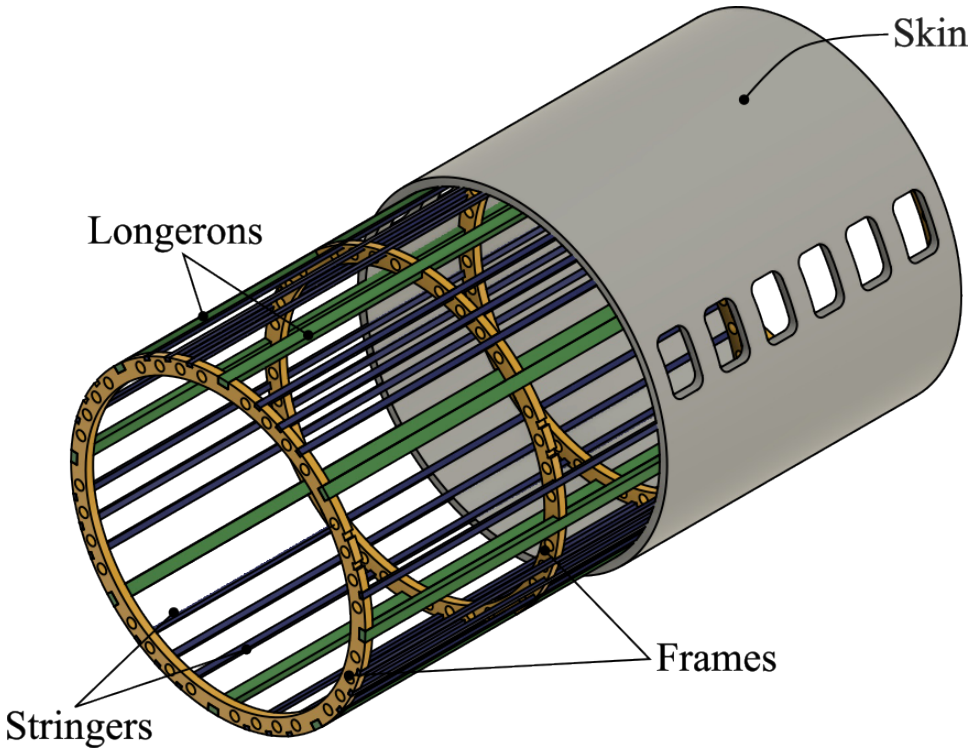


Figure 2.4 Standard aircraft fuselage with key structural components: stringers, skin, longerons and frames

When the fuselage is constructed with conventional materials such as aluminum, the fuselage is assembled from multiple panels, which are then riveted to the stringers and frames to form the overall structure. These stringers and frames provide the necessary stiffness to withstand the various loads acting on the aircraft.

As a result, this approach, commonly referred to as stiffened panel design, allows optimization by adjusting the material properties, geometric dimensions, spacing and orientation of the skin, stringers and frames to achieve a high stiffness-to-weight ratio. These panels also enable the automation of various assembly operations by dividing the overall aircraft structure into modular segments. As illustrated in Figure 2.3, instead of relying on a monocoque shell, incorporating stringers and frames as stiffeners helps prevent buckling while maintaining a thin and lightweight outer skin. Figure 2.5 illustrates common stringer geometries found in aircraft structures.

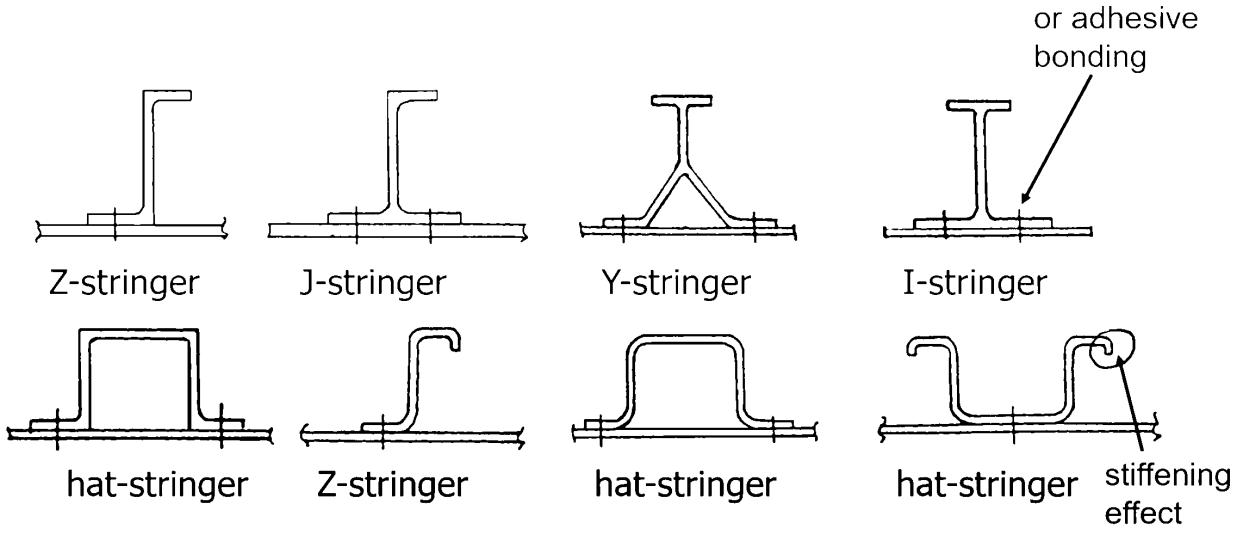


Figure 2.5 Stiffener geometry commonly used in aerospace application [14]

The specific load conditions influence the selection of stiffeners for different parts of the aircraft in each location. Factors such as cost, weight, and availability also play crucial roles in determining the appropriate stiffener type. Another design variable in the stiffened shell structures of aircraft is the orientation of the stiffeners related to frames. The most common types of orientation are orthogrid and isogrid as shown in Figure 2.6. The orientation will depend on a compromise between design requirements, manufacturing, and cost. Ortho-grid configuration use the frame pitch "$a$" and stiffener pitch "$b$" as design variables. For the iso-grid configuration, the frame pitch "$a$", stiffener pitch "$b$" and stiffener angle "$\alpha$" are used. Each configuration requires the definition of two independent parameters.

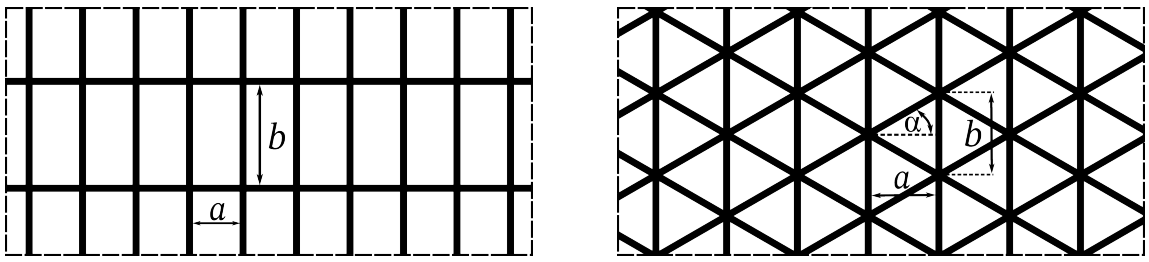


(a) Ortho-grid configuration (b) Iso-grid configuration

Figure 2.6 Difference between ortho-grid and iso-grid stiffened panels configuration adapted from [17]

The ortho-grid configuration, shown in Figure 2.6a and Figure 2.4, is typically preferred due

to its manufacturing advantages over the iso-grid structure. The selection of this configuration and its associated geometrical parameters depends on the results of the finite element analysis (FEA) during the aircraft's design phase.

### Wing Design

The wing plays a critical role in enabling flight by generating lift and housing control surfaces such as flaps and ailerons. Given their size, wings must also achieve an optimal strength-to-weight ratio to efficiently transfer part of the load path to the fuselage while keeping the aircraft's mass low. The most commonly used semi-monocoque wing structure consists of ribs, stringers, and spars as the internal framework beneath the skin, as shown in Figure 2.7.

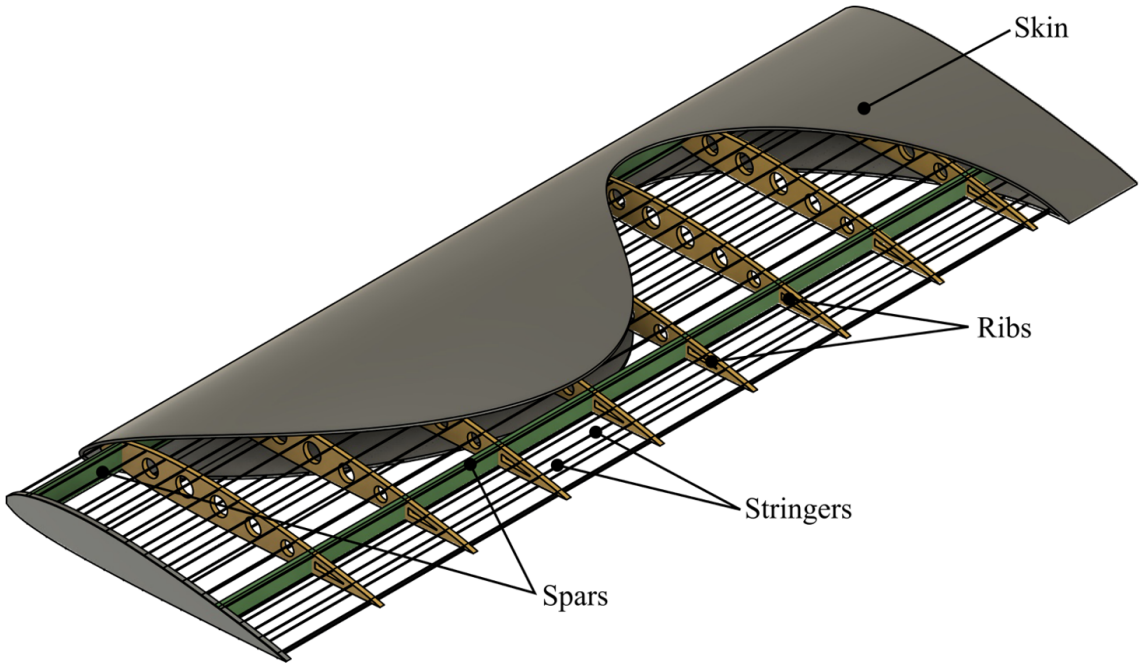


Figure 2.7 Typical semi-monocoque wing structure showing key components: skin, ribs, stringers and spars

The spar acts as a rigid longitudinal membrane through the wing, similar to the longeron in the fuselage. The ribs help maintain the wing's aerodynamic shape and prevent buckling, functioning similarly to the frames in the fuselage. The shape and orientation of these structural elements can be defined during the design phase using FEA, in combination with the expertise and experience of structural engineers.

## 2.2 Evolution of Blended Wing Body Aircraft and its Structural Design

The emergence of BWB aircraft marks a major breakthrough in aerospace, seamlessly integrating the wing and fuselage to improve both performance and efficiency. This section first explores the BWB concept and its evolution, emphasizing its departure from traditional designs and the vision behind its development.

The origins of the BWB can be traced back to the early aspirations of achieving a more efficient wing design that could incorporate the fuselage as a load-bearing component, thus reducing drag and improving performance. This idea evolved, influenced by advancements in aerodynamic theories and materials science. The concept gained significant traction in the late 20th century as environmental concerns and rising fuel costs prompted a reevaluation of conventional aircraft designs. In response to this new paradigm, McDonnell Douglas engineer Robert Liebeck drafted an initial concept for an aircraft with reduced fuel consumption as seen in Figure 2.8 [18].

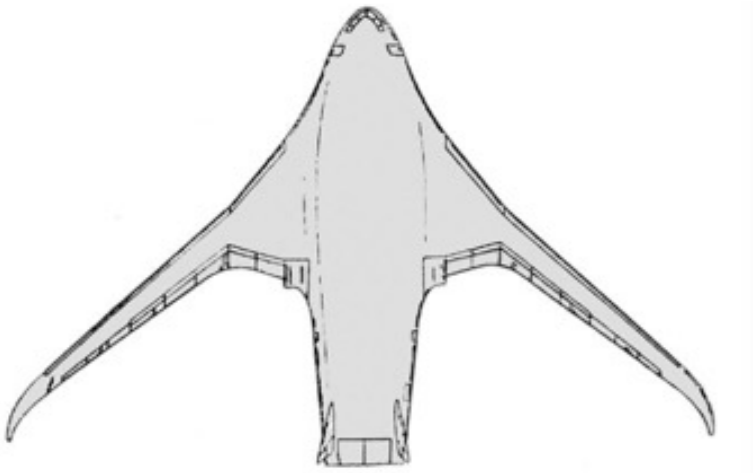

Figure 2.8 Robert Liebeck's early 1988 BWB concept sketch [19]

Initial theoretical studies and small-scale experiments demonstrated the potential of the BWB design to achieve superior lift-to-drag ratios compared to traditional designs. This led to more focused research initiatives, particularly by NASA and major aerospace companies like Boeing and McDonnell Douglas. Following the merger of McDonnell Douglas and Boeing in 1998, the focus for BWB shifted from earlier 800-seat concepts to a lower capacity 450-seat design, designated as BWB-450 [20]. The collaboration aimed at addressing the complex challenges posed by the BWB configuration, such as stability, control, and integrating systems within a non-traditional airframe. The development process included extensive

computational modeling and wind tunnel testing, which were essential to refining the design and confirming its aerodynamic advantages. The study [21] also showed a structural layout for the BWB from the X-48 research as shown in Figure 2.9.

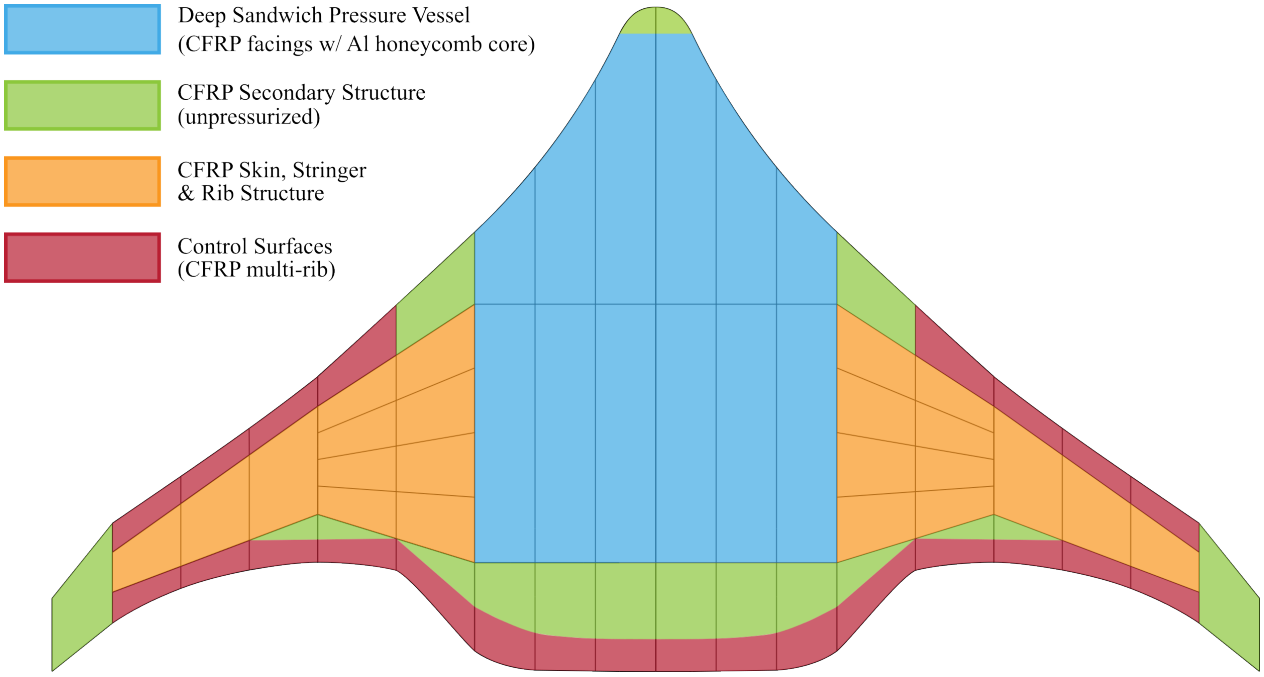


Figure 2.9 X48B strucural layout developped by NASA. Adapted from [21]

The wings of the X48B utilize a conventional semi-monocoque structure, incorporating a skin, stringers, and ribs similar to those found in TAW aircraft. The leading edge of the fuselage features a 5-inch-thick CFRP honeycomb core sandwich structure, reinforced with vertical walls to withstand pressure induced by the aircraft's geometry, as explained in Section 1.2.3. In contrast, the trailing edge of the fuselage employs a standard CFRP skin structure, as it is not subject to pressurization. Additionally, NASA investigated a conventional semi-monocoque fuselage stiffened with stringers and frames, concluding that it represents a competitive structural solution.

After six years of flight testing and data collection, the project came to an end in 2013, having fulfilled it's experimental objectives. The X-48 aircraft concept proved highly promising in supporting NASA's environmental goals for future aircraft designs [22]. In the following years, several concepts emerged, drawing inspiration from NASA's research but with a stronger emphasis on optimizing the aerodynamics of BWB aircraft throughout the 2010s [23].

The 2020s decade began with a significant acceleration in the development of BWB designs for both commercial and private applications. This is mainly due to the ambitious goal of

net zero carbon emission by 2050 set by the International Air Transport Association (IATA) at the 77th IATA Annual General Meeting in Boston in October 2021 [6]. Many aircraft manufacturers such as Airbus, Boeing, Bombardier and Jetzero are currently (2025) working on BWB design for future industrial applications as we can see in Figure 2.10.

(a) MAVERIC by Airbus (b) EcoJet by Bombardier (c) Pathfinder by JetZero

Figure 2.10 Multiple BWB concepts revealed in the early 2020s [24–26]

As illustrated in Figure 2.10, the Maveric and Pathfinder concepts were introduced in 2020 and 2023, respectively, with a focus on commercial airline applications, while the EcoJet, announced in 2023, is designed for private jet use. Despite their differing target markets, these concepts share fundamental characteristics inherent to the BWB configuration. By seamlessly integrating the wing and central fuselage, they depart from traditional TAW aircraft designs to enhance aerodynamic efficiency and improve fuel economy.

## 2.3 Topology Optimization for Structural Design

Topology optimization (TO) based on Finite Element Analysis (FEA) is a powerful technique that helps structural engineers identify the optimal material distribution within a defined design space. Among the various methods available, the Solid Isotropic Material with Penalization (SIMP) approach is the most widely implemented in commercial software. Other promising TO algorithm has been explored by our research group such as the Moving Morphable Components [27] and the Ground Structure Method [28]. This section introduces the SIMP method and outlines key metrics for assessing the quality of TO results, as it is the technique our team chosen for this research for it's integration into existing FEA software such as Altair HyperMesh.

### 2.3.1 Introduction to Solid Isotropic Material with Penalization

The SIMP method is a TO approach based on density distribution. The design space is discretized into small elements, and the optimization process results in each element having a density $\rho_e$, where $\rho_e \in [0, 1]$.

Compliance is a measure of the flexibility of a structure under applied loads. It is the work done by the external forces on the structure's displacements. Mathematically, compliance is given by:

$$f(\rho) = \mathbf{u}^T \mathbf{K}(\rho)\mathbf{u}, \tag{2.3}$$

where $\mathbf{u}$ is the displacement vector, $\mathbf{K}(\rho)$ is the global stiffness matrix dependent on the material distribution $\rho$, and $\mathbf{u}^T\mathbf{K}(\rho)\mathbf{u}$ represents the strain energy in the structure.

The optimization problem can be formulated as:

$$\begin{aligned}
\text{minimize compliance} \quad & f(\rho) = \mathbf{u}^T \mathbf{K}(\rho)\mathbf{u} && (2.4)\\
\text{subject to} \quad & \mathbf{K}(\rho)\mathbf{u} = \mathbf{F}, && (2.5)\\
& V(\rho) \leq V_{\max}, && (2.6)\\
& 0 \leq \rho_e \leq 1 \quad \forall e, && (2.7)
\end{aligned}$$

where $\mathbf{F}$ is the force vector representing the external loads, $V(\rho)$ is the volume of the material used, and $V_{\max}$ is the maximum allowable volume.

### 2.3.2 Density Based Topology Optimization Application in Structural Design

When using commercial design software, designers begin by defining the design space, which originates from the CAD file and is then represented as a mesh composed of multiple elements, depending on the chosen mesh size. Next, boundary conditions are applied to reflect the real-world application of the design parts into the design space. These conditions include displacement constraints related to $\mathbf{u}$, forces, moments, and pressure related to $\mathbf{F}$ in the FEM equation. All these steps are mandatory to perform a linear static analysis.

Next, the user can setup the TO problem to get a better understanding of the loadpath leading to the selection of an optimal material distribution. The optimization problem needs

at least one constraint and one optimization variable. In most case, the goal is to minimize compliance under a maximum volume constraint as explained previously.

Figure 2.11 shows the density of some elements relative to the original rectangular design space. In this case, it is evident that the topology optimization resulted in a more truss-shaped design, which is optimal for maximizing the stiffness of the beam while minimizing mass distribution. Additional constraints can be defined, such as minimum and maximum member sizes, symmetry, and pattern repetition. These constraints vary depending on the specific problem being addressed and may include design requirements like fatigue resistance, buckling resistance, or manufacturability.

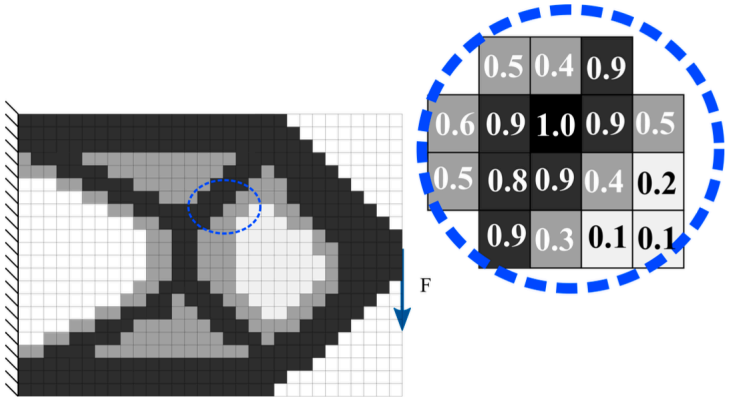


Figure 2.11 Visualization of SIMP Algorithm elements density. The values represent each element density $\rho_e$ of each element, changing the overall stiffness of the corresponding structure. The force F is applied at the center of the right edge of the design domain [29]

### 2.3.3 Metrics for Evaluating Density based Topology Optimization Results

One common way to assess the quality of SIMP results is by examining the final objective value at the end of the optimization. The solution typically starts at an initial compliance value and converges to a local minimum that satisfies the objective and constraints. However, other metrics have been used, as seen in this study [30], where SIMP methods were compared both among themselves and against other TO algorithms.

In this article, the quality of the results was quantified using several criteria. The mean member size was evaluated to assess manufacturability, ensuring that the generated structures were feasible for fabrication with traditional technologies. The objective function value was used to determine how well each method minimized the absolute compliance. The number of iterations and CPU time were measured to compare computational efficiency. Additionally,

the robustness of the solutions was analyzed by checking the convergence behavior and stability of the topology across different optimization runs. One conclusion drawn was that the SIMP method represents the most widely adopted topology optimization approach, valued for its robustness and efficiency in large-scale problems, although it often relies on filtering techniques to reduce gray regions and enhance manufacturability.

### 2.3.4 Superposing Solutions to Identify Patterns in Topology Optimization Results

When input constraints are modified in the optimization process, the results can differ significantly. The optimal solution is sometimes revealed through repeated patterns across multiple results, where certain load paths appear more frequently than others, as illustrated in Figure 2.12c. The overlapping regions represent the solution where pixels from topology A and topology B consistently exhibit high-density values at the same locations. This approach aids in identifying an optimal load path when analyzing a range of optimization outcomes.

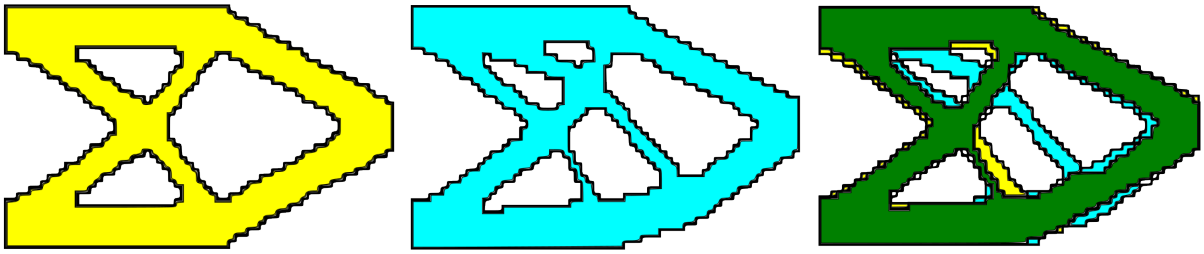

(a) Optimized Topology A (b) Optimized Topology B (c) Overlap region of A and B

Figure 2.12 Repetition of patterns in TO results under varying hole number constraints. Adapted from [31]

## 2.4 Topology Optimization in the Aircraft Design Process

TO can be integrated into the design process to develop weight-efficient structures. Unlike in the past, engineers no longer have to rely solely on intuition and experience to effectively distribute material within a given geometry to ensure an optimal load path. In aircraft design, TO can be utilized to accelerate the design phase, from individual elementary parts to the overall structural architecture.

### 2.4.1 Interpreting an Optimal Topology to Determine the Aircraft Structure

TO can also be applied to global aircraft structure, such as a section or the entire fuselage. The process is similar for components like brackets, but the results require more complex interpretation. In the context of global aircraft structure, TO results can provide the optimal distribution of stiffeners and frames throughout the aircraft.

In [32], a global structural TO process is presented for the center fuselage using the Altair's HyperMesh OptiStruct engineering tool. The process begins by interpreting the boundary conditions based on the aircraft's geometry. Next, the optimization parameters are defined, and the TO procedure is executed on the FEM model of the center fuselage. The resulting topology is then refined by standardizing the structure to simplify the design and manufacturing, as illustrated in Figure 2.13. It is important to mention that the skin is not optimized during the TO.

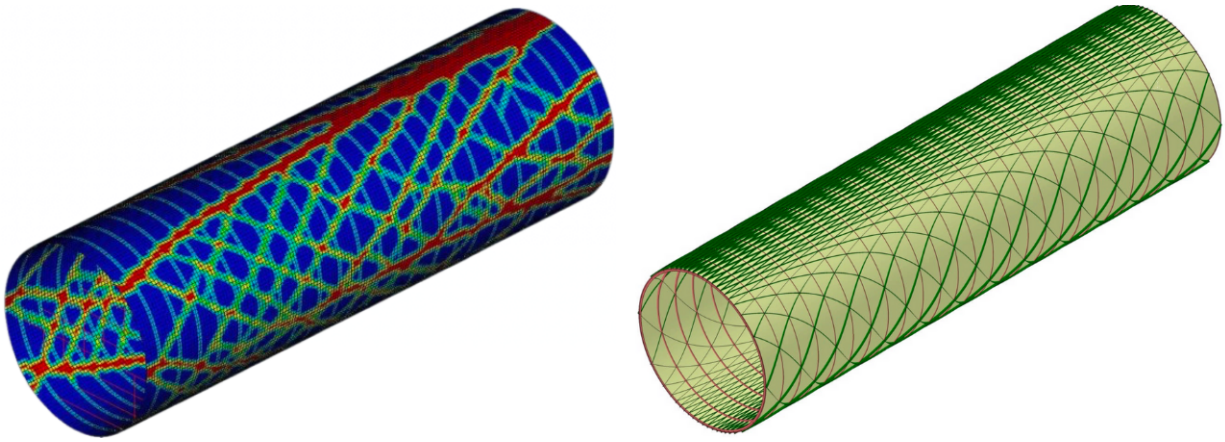

(a) TO results from HyperMesh (b) Subsequent CAD interpretation

Figure 2.13 Optimal material distribution for a center fuselage from global architecture TO : (a) TO results from HyperMesh, (b) Subsequent CAD interpretation. The color map in (a) indicates the density of each element, with red representing a density of 1 (material is necessary for optimal distribution) and blue representing a density of 0 (material is not needed) [32]

As shown in Figure 2.13a, most stiffeners exhibit a helicoidal rotation around the roll axis of the fuselage which is chosen to an iso-grid pattern. The membranes from the TO results form a primary angle $\alpha$ of 38 degrees relative to the longitudinal plane. This angle is then used to derive the interpretation of the optimal stiffening layout, illustrated in Figure 2.13b.

### 2.4.2 Using Topology Optimization as a Design Tool for Determining the Aircraft Optimal Structure

Another approach explored by Stelia is to directly use the TO results to define the spacing and orientation of the stiffeners. A subsequent sizing optimization is then performed to determine the dimensions of structural components such as the skin, stringers, and frames [33]. Figure 2.14 illustrates the optimal material distribution for the front fuselage used in this study.

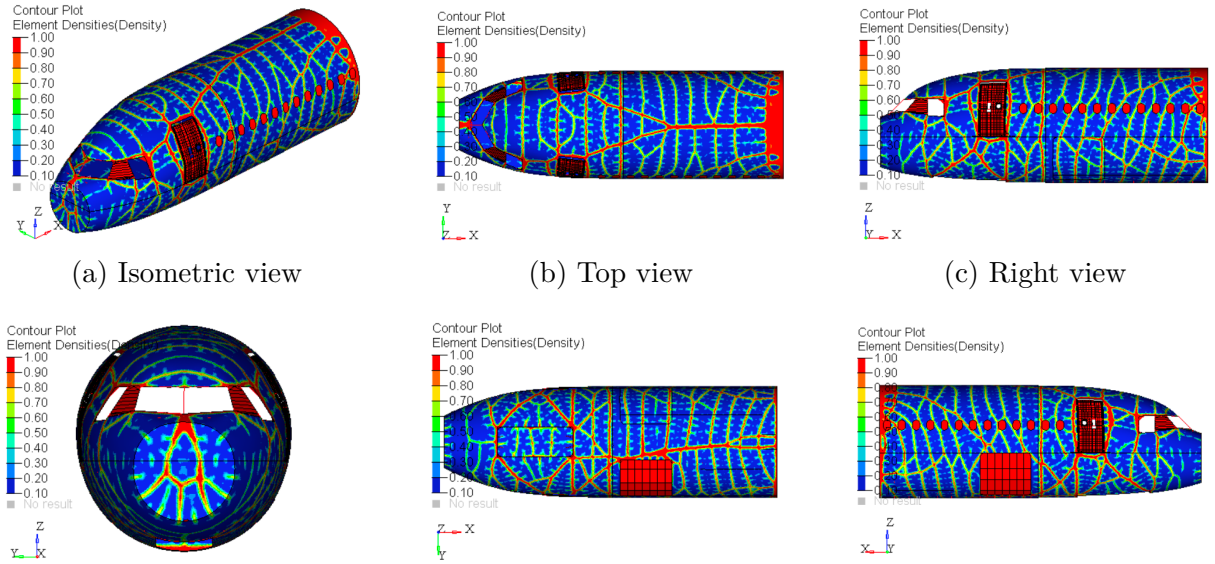


(a) Isometric view (b) Top view (c) Right view

(d) Front view (e) Bottom view (f) Left View

Figure 2.14 Optimal material distribution for a front fuselage from global structure TO developed by Stelia Aerospace [33].

Certain regions, such as the windows and landing gear bay, are defined as non-design spaces. Their density is fixed at full value and excluded from the optimization process. However, they can still support loads and be subjected to boundary conditions. The red membrane highlights the optimal stiffener placement, while the blue areas can remain as skin-only regions, following the same design approach used for the center fuselage in [32]. These TO results provide guidance for obtaining a fuselage structure with minimal modifications from the original optimization outcomes, as shown in Figure 2.15.

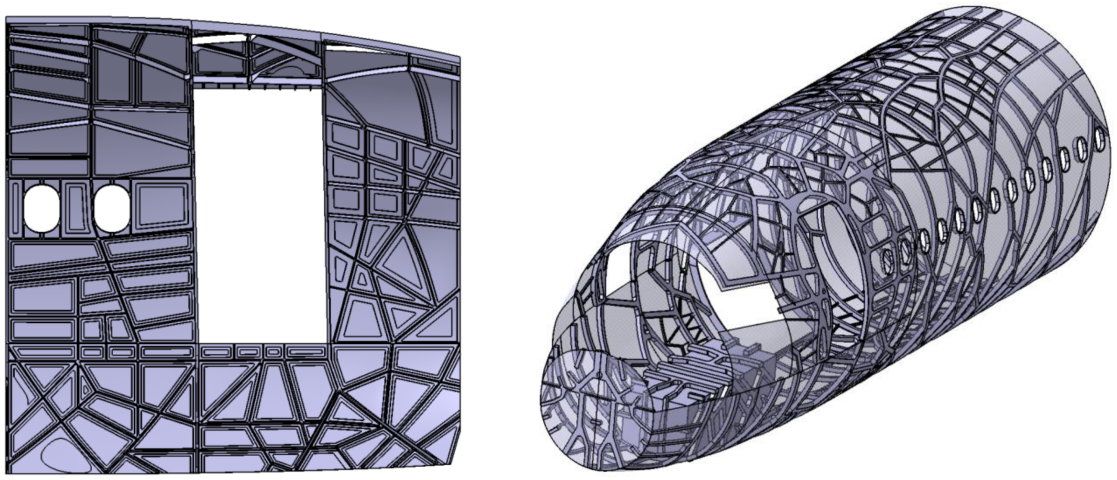

(a) Inside view (b) Isometric view

Figure 2.15 The front fuselage structure derived from previous TO [33]

The stiffening layout for the design concept shown in Figure 2.15 is primarily based on the optimization results from Figure 2.13, which guide the optimal material distribution to maximize stiffness while adhering to mass constraints. However, from a manufacturing perspective, the stiffener distribution is not ideal, as it would require components of varying sizes and shapes. Stelia Aerospace explored machining and additive manufacturing techniques to produce these custom panels, but this remains an early-stage concept that is not yet cost-effective [34].

The potential of TO extends to other parts of the aircraft as well, such as the wing structure. A high-resolution voxel-based TO applied to a full-scale wing, comparable to that of the Boeing 777, illustrates the level of precision and scale that can now be achieved in optimizing complex aerospace structures [35], as shown in Figure 2.16. This approach showcases how TO can reduce material usage in wings structure while maintaining structural integrity, offering promising benefits for future aircraft designs.

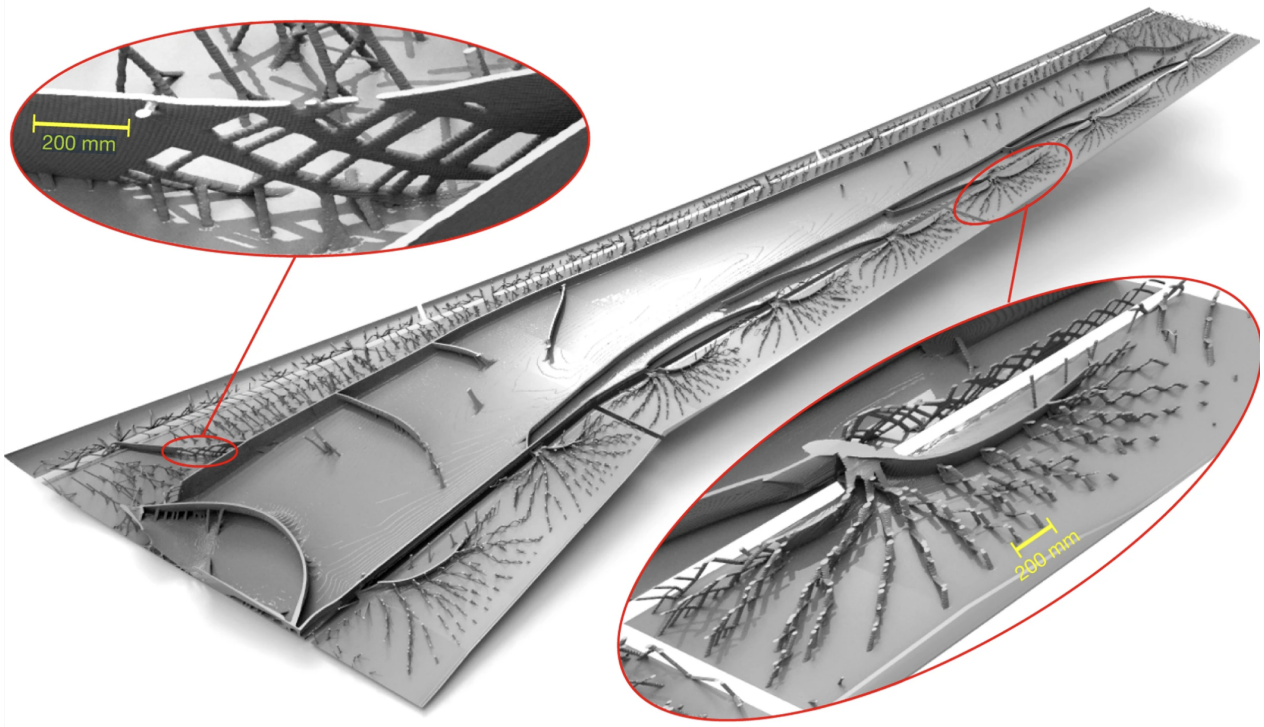


Figure 2.16 High-resolution TO results for a full-scale wing comparable to that of the Boeing 777 [35]

The high-resolution TO results demonstrate a stiffened skin that integrates aspects of both monocoque and semi-monocoque structures, with the skin absorbing stress and distributing loads to other parts of the aircraft. The primary stiffeners resemble the spars found in typical semi-monocoque wing designs, as discussed in Section 2.1.3. Additionally, the study compared the wing structure to the organic wings of the Hornbill bird, uncovering numerous similarities. TO presents the opportunity to mimic nature's designs, pushing aircraft development into a new era.

## 2.5 Litterature Review Summary and Problem Definition

The BWB aircraft has emerged as a promising alternative to conventional TAW configurations, offering improved aerodynamic efficiency and fuel savings. While the aerodynamic benefits of BWB designs are well-documented in the literature, their internal structural architecture remains largely unexplored. Traditional aircraft structures, such as monocoque and semi-monocoque designs, have well-established methodologies for material selection, load distribution, and buckling resistance. However, due to the unconventional geometry of BWB aircraft, these traditional design principles may not be directly applicable. NASA's research

on BWB structures has proposed using CFRP sandwich panels for the fuselage and conventional semi-monocoque structures for the wings. However, there is still limited documentation on how aerodynamic loads influence the internal structure of BWB aircraft.

The inclusion in the design process of TO has gained significant attention and traction in the aerospace industry for its ability to generate lightweight, high-performance structures [33]. However, its inclusion in the design process to full-scale aircraft structural design remains limited, particularly for unconventional configurations like the BWB. The literature lacks a quantifiable measure for evaluating the quality of TO-generated results in aircraft structures, especially when using commercial finite element software. Developing a metric to assess TO results could help streamline the selection of optimal structural solutions and improve design efficiency.

Furthermore, there is limited established methodology for using TO to determine the optimal internal structure of BWB aircraft. While TO has been successfully applied to smaller components and conventional aircraft sections, its extension to BWB configurations requires new approaches to account for unique load paths. Establishing a structured methodology for applying TO to BWB aircraft along with a framework for evaluating its results could significantly enhance structural design processes and facilitate the adoption of BWB configurations in the aerospace industry. This raises the following research question: How can structural engineers be effectively supported in applying TO to BWB structures in early design phase?

## 2.6 Research Objective

**Main Objective (MO)**: Develop a framework to support structural engineers determine the optimal stiffening patterns for a BWB aircraft structure using TO.

**Sub-Objectives (SO)**:

**SO1**: Develop a performance metric to select the best TO result with respect to structural compliance and interpretability.
**SO2**: Determine the optimal stiffener layout of a BWB using TO results under multiple loading scenarios.
**SO3**: Develop a visual guideline for the execution of the developed framework.

## 2.7 Summary of the Methodology

1. **Evaluating the structural performance and Interpretability of TO Results**: Derive a performance metrics based on TO outputs to quantitatively assess structural

stiffness and design interpretability. **(SO1)**

2. **Validating the Developed Metrics**: Assess the proposed evaluation metrics by applying them to TO results from a well-documented scientific case study. Verify the reliability of the performance metric through expert review in the density-based TO domain. **(SO1)**

3. **Creating a Finite Element Model for a Blended Wing Body Aircraft**: Build a representative finite element model that incorporates the overall geometry and specific boundary conditions to simulate aerodynamic loads: wing up-bending, dynamic landing, roll maneuvers, and engine thrust. **(SO2)**

4. **Implementing TO Algorithms**: Perform multiple TO runs for each load case and determine the best overall design using the previously developed performance metric. **(SO2)**

5. **Comparative Analysis of TO Results**: Analyze the optimized results for each loading scenario to evaluate performance and identify the most efficient configurations. **(SO2)**

6. **Developing a Visual Execution Guideline for the Framework**: Construct a flowchart of the entire methodology pipeline, from TO setup and performance evaluation to stiffener layout selection. **(SO3)**

# CHAPTER 3 DEVELOPMENT OF A PERFORMANCE METRIC FOR DENSITY-BASED TOPOLOGY OPTIMIZATION RESULTS

In this section, we will focus on SO1 by developing a FEA to assign a quantitative score to density-based TO results, utilizing data from advanced software. Altair HyperMesh is used for this research. This scoring system will provide an objective means of evaluating TO outcomes, facilitating the selection of the most optimal design based on predefined criteria. Ultimately, this methodology will be extended to more complex structures, including the global structure supporting the BWB aircraft, as part of SO2.

### Reason behind a performance metric

Evaluating TO results to determine the best solution for a specific application is challenging because it often depends on the expertise of multiple engineers throughout the design process. The ultimate goal of TO is to streamline design by identifying the optimal load path for a structure. The resulting design must adhere to optimization constraints, such as minimizing compliance to maximize stiffness, and be interpretable by designers for manufacturing.

Determining the optimal topology for stiffness and interpretability from Table 3.1 is a complex task, as assessing the extent to which one topology outperforms another requires careful analysis. This challenge highlights the importance of a quantitative approach for objective evaluation.

Table 3.1 Diverse results from TO of a cantilever beam

| Result No 1 | Result No 2 | Result No 3 |
|---|---|---|
| 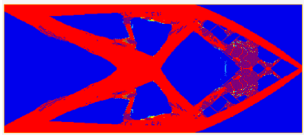 | 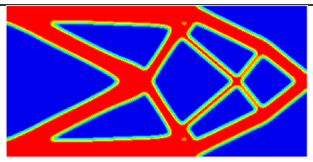 | 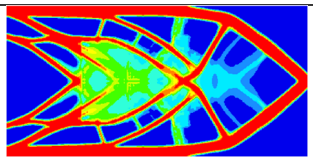 |

By the end of this chapter, we will be able to assign a quantitative score to each TO result from Table 3.1, allowing us to objectively compare their relative performance.

Previous research within the research group evaluated the complexity of density-based TO results [36]. However, it did not focus on establishing a relative score for interpretability and stiffness, which we will address in this chapter.

In [30], various TO methods were compared using performance indicators such as total iterations, objective function (compliance), and average member size. This gives an overview of some possible indexes to look for in a structural TO performance evaluation.

### 3.1 Model Description : Cantilever Beam

To identify TO performance indicators, the well-known cantilever beam shown in 3.1, widely used in previous studies due to its simplicity, will be employed. Despite its straightforward design, it offers a range of interesting features for exploration.

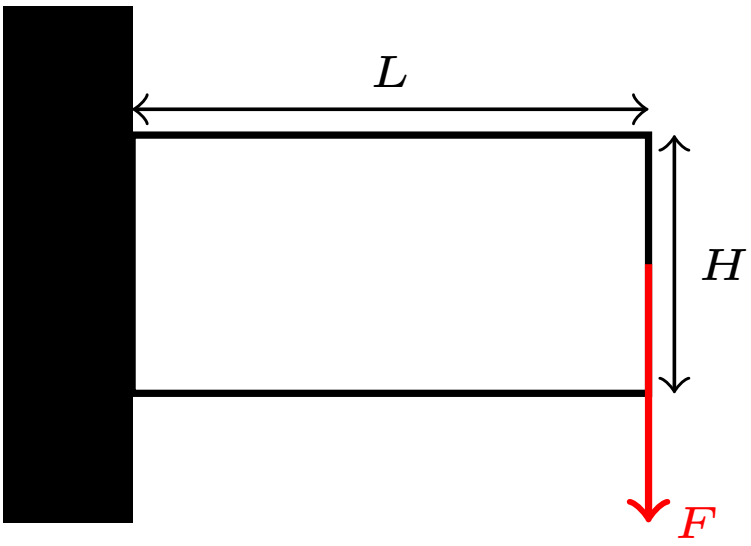


Figure 3.1 Schematic of a Cantilever Beam of Length $L$ and Height $H$ Under Force $F$

The dimensions of the Cantilever Beam will be $L = 200mm$ and $H = 100mm$. The force used is $F = 1000N$. The remaining volume fraction after the optimization is set to 40% as it is a good balance between mass reduction and structural performance.

The optimization problem can be formulated as:

$$\begin{aligned} \text{minimize compliance} \quad & f(\rho) = \mathbf{u}^T \mathbf{K}(\rho)\mathbf{u} && (3.1)\\ \text{subject to} \quad & \mathbf{K}(\rho)\mathbf{u} = \mathbf{F}, && (3.2)\\ & V(\rho) \leq V_{\max} = 40\%, && (3.3)\\ & 0 \leq \rho_e \leq 1 \quad \forall e, && (3.4) \end{aligned}$$

where $\mathbf{F}$ is the force vector representing the external loads, $V(\rho)$ is the volume of the material used, and $V_{\max}$ is the maximum allowable volume.

### 3.2 Mesh Convergence Analysis

The cantilever beam is meshed exclusively with QUAD4 elements due to its rectangular 2D geometry.

It is crucial to verify that the results are not mesh-dependent. A reliable approach is to perform TO for a specific load case, refining the mesh by halving its size until the value of interest, compliance in our case varies by less a defined value. We must also consider the minimum member size in the TO process, as ensuring numerical stability requires a mesh size that is three times smaller [37]. For this example, we select an arbitrary minimum member size of 2 mm, which means the average mesh size should not be coarser than 0.67 mm to satisfy the numerical stability requirements as shown in Figure 3.2.

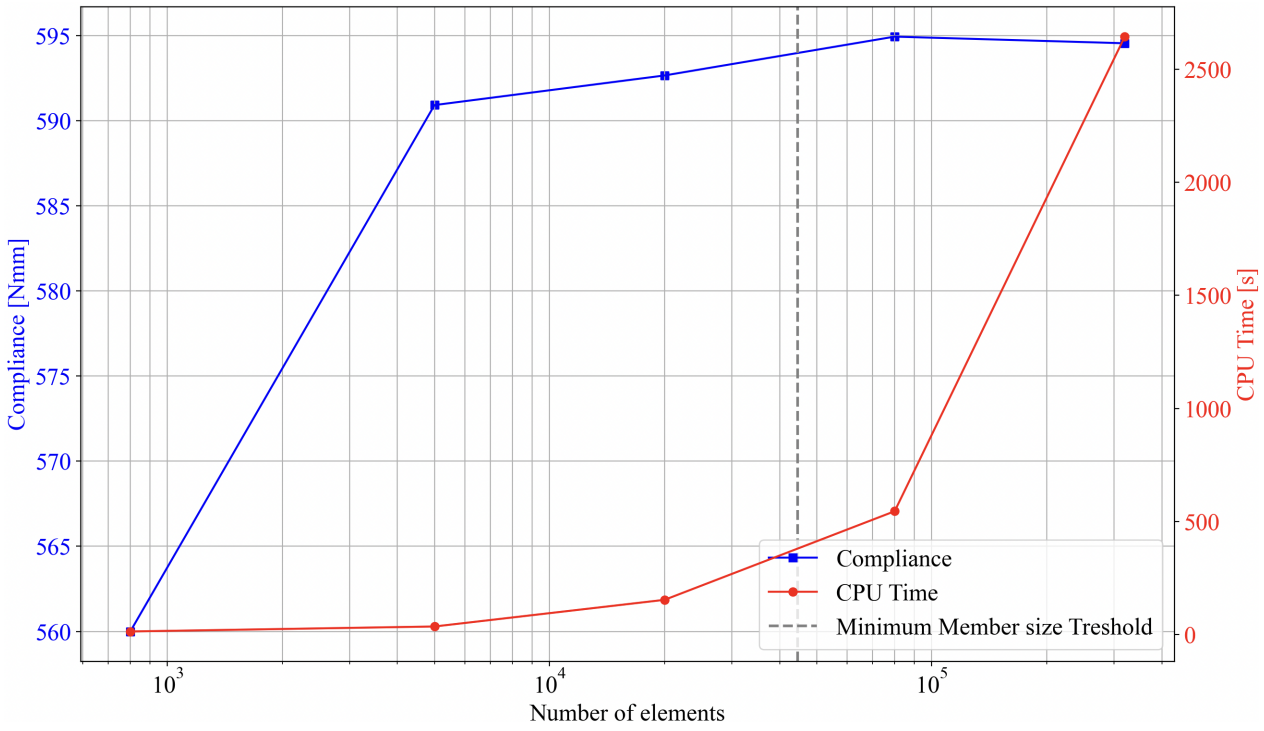


Figure 3.2 Mesh convergence analysis for the TO of the Cantilever Beam from Figure 3.1

In this scenario, a mesh size of 80,000 elements was chosen, as increasing to 320 000 elements results in only a 0.065% difference in compliance while significantly increasing CPU time by 385%. The 80 000-element mesh uses QUAD4 elements with a size of 0.5 mm, which is

smaller than the 0.67 mm required to satisfy the minimum member size constraint.

### 3.3 Optimization Inputs and Extracted Metrics

Altair HyperMesh provides significant flexibility for configuring complex TO to meet specific requirements. In our study, we will modify various TO input parameters to examine their impact on the results and key metrics as shown in Figure 3.3.

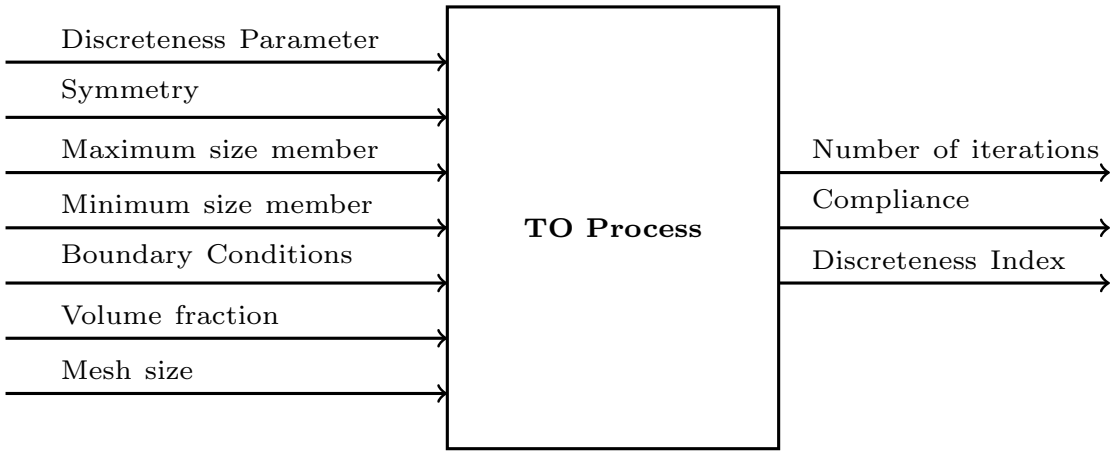


Figure 3.3 TO inputs and extracted metrics

The minimum member size (MINDIM) and maximum member size (MAXDIM) parameters constrain the algorithm by defining the smallest and largest allowable structural features. The discreteness parameter (DP) affects the penalization factor in the SIMP method, influencing the material distribution. Additionally, the symmetry (SYM) constraint ensures that the TO result remains symmetric about the beam's centerline and perpendicular to the applied force. In TO, the symmetry constraint serves as a pattern repetition parameter, not a geometric simplification. Specifically, it ensures that the densities of corresponding elements across the axis of symmetry remain equal throughout the optimization process, thereby enforcing a mirrored material distribution. This promotes interpretable and balanced designs, but does not reduce the size of the model or the number of degrees of freedom as in traditional FEA symmetry constraints.

### 3.4 Performance Indicators

The objective of this study is to establish a benchmark to differentiate various TO results performance. We aim to measure both the stiffness of the structure (through compliance)

and its manufacturability or interpretability (through the Discreteness Index (DI)). A design with high stiffness (low compliance) but low DI (poor interpretability), or a design with high interpretability but low stiffness, is not ideal. Our goal is to achieve a balance, where the design is both stiff and interpretable.

### Discreteness Index

The DI represents the ratio of well-defined element densities to intermediate densities in the optimization results. It is mathematically describe as :

$$DI = \frac{\sum_{e=1}^{n} (\rho_e V_e), \quad \text{if} \quad 0.9 \leq \rho_e \leq 1.0}{\sum_{e=1}^{n} (\rho_e V_e)} \tag{3.5}$$

where $\rho_e$ and $V_e$ are the density and Volume of each element $e$.

In TO, element densities $\rho_e$ range from 0 to 1, where 0 indicates the absence of material and 1 signifies full material presence. Intermediate densities are less significant from a design standpoint, as their optimization does not clearly indicate how to enhance the structure effectively. Figure 3.4 presents an example illustrating two distinct topologies obtained after the optimization process, showing a significant difference in DI values.

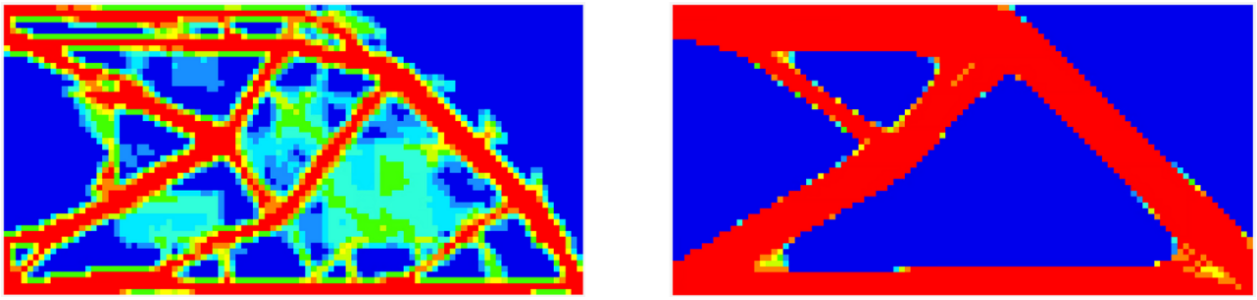

(a) 48% DI (b) 92% DI

Figure 3.4 Difference between the DI of two TO results for the same load case and a consistent volume fraction constraint of 40%

As seen in Figure 3.4, there is a significant difference in the DI values between each TO result, with (b) being more straightforward to interpret for manufacturing purposes. The DI can be regarded as an interpretability index related to manufacturability, assisting structural engineers understand the material distribution and guiding the design process accordingly.

### Stiffness Score

One challenge is that the compliance formulation of a specific TO result does not provide a clear relative score. The compliance value will vary depending on the geometry and boundary conditions. To address this, we can evaluate the compliance range for a specific volume fraction and load condition by determining the maximum and minimum compliance that is achievable in our design space. By interpolating between these two extremes, we can assess where our design stands in terms of stiffness, relative to the highest and lowest values obtainable as illustrated in Figure 3.5.

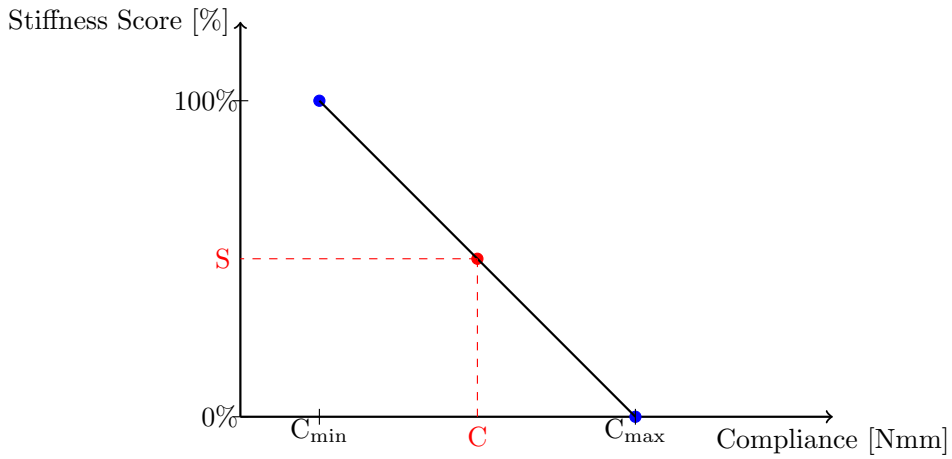


Figure 3.5 Stiffness score interpolation for a specific load case and volume fraction

The stiffness score S can be linearly interpolated :

$$S = (1 - \frac{C - C_{min}}{C_{max} - C_{min}}) * 100 \tag{3.6}$$

Maximum stiffness, thus minimum compliance $C_{min}$, is achieved when all element densities $\rho_e$ are set to 1, corresponding to a score of 100%. In contrast, the minimum stiffness, represented by a score of 0%, occurs when the design is highly flexible, which means that compliance is maximized. For a given volume fraction, $C_{max}$ is found at the beginning of the optimization process, when all densities $\rho_e$ are uniformly set to the initial volume fraction constraint. If the optimization process fails to converge, meaning that the final compliance $C$ exceeds the reference maximum compliance $C_{max}$, the stiffness score is set to 0% to avoid dealing with negative score cases.

## 3.5 Resulting Topologies of the Optimized Cantilever Beam

33 TO results were generated by varying the input parameters for the cantilever beam. Table 3.3 displays the resulting topologies corresponding to the four specified inputs. Table 3.4 presents the resulting topologies alongside the number of optimization iterations and the performance indicators defined in Section 3.4. Each table displays a sample of 10 results to enhance readability in this section.

Table 3.3 TO Inputs with Resulting Topology. Red pixels indicate the highest density value of 1, blue pixels correspond to the lowest density value of 0, and intermediate colors represent values between these two extremes

| Result No. | MINDIM [mm] | MAXDIM [mm] | SYM | DP | Resulting Topology |
|---|---|---|---|---|---|
| 1 | N/A | N/A | N/A | 1 | 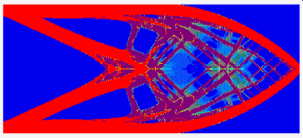 |
| 2 | N/A | N/A | N/A | 2 | 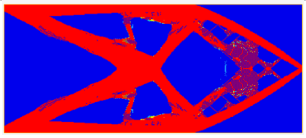 |
| 3 | 2 | N/A | N/A | 1 | 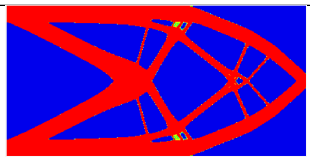 |
| 4 | 9 | N/A | N/A | 2 | 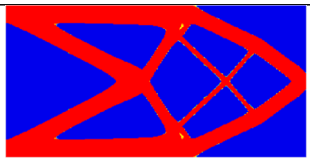 |
| 5 | 12 | N/A | N/A | 1 | 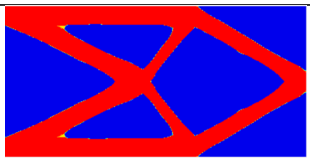 |
| 6 | 6 | 30 | YES | 1 | 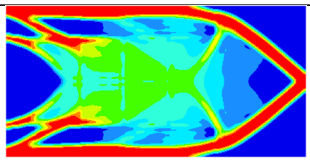 |

| Result No. | MINDIM [mm] | MAXDIM [mm] | SYM | DP | Resulting Topology |
|---|---|---|---|---|---|
| 7 | 6 | 50 | YES | 1 | 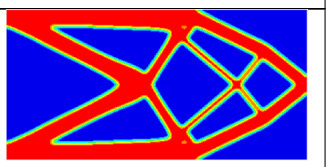 |
| 8 | 12 | 50 | YES | 1 | 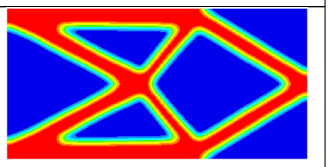 |
| 9 | 6 | 18 | YES | 1 | 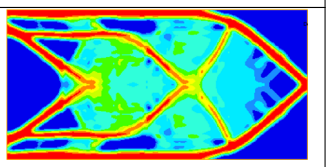 |
| 10 | 3 | 30 | YES | 1 | 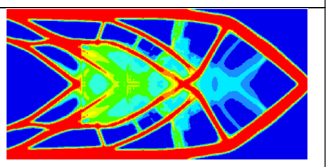 |

Table 3.4 Resulting Topology with number of iterations and performance indicators. Red pixels indicate the highest density value of 1, blue pixels correspond to the lowest density value of 0, and intermediate colors represent values between these two extremes

| Result No. | Resulting topology | Number of Iterations | DI [%] | Stiffness Score [%] |
|---|---|---|---|---|
| 1 | 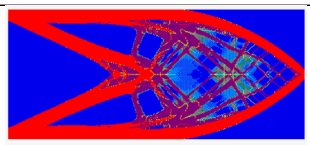 | 59 | 91.0 | 82.8 |
| 2 | 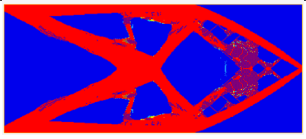 | 32 | 98.0 | 77.8 |
| 3 | 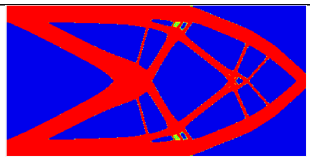 | 75 | 98.0 | 82.9 |

| Result No. | Resulting topology | Number of Iterations | DI [%] | Stiffness Score [%] |
|---|---|---|---|---|
| 4 | 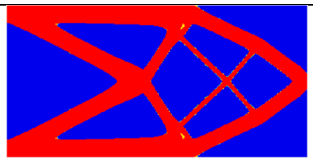 | 89 | 98.0 | 83.6 |
| 5 | 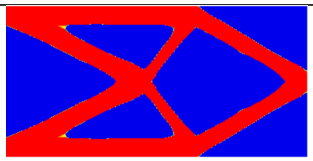 | 103 | 98.0 | 83.5 |
| 6 | 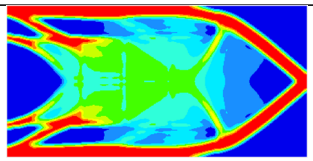 | 80 | 35.0 | 15.1 |
| 7 | 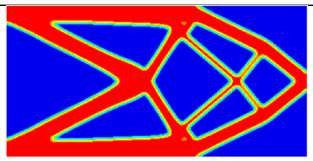 | 62 | 74.0 | 77.4 |
| 8 | 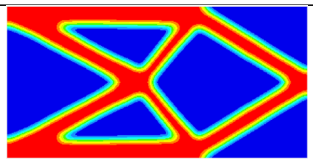 | 73 | 61.0 | 71.6 |
| 9 | 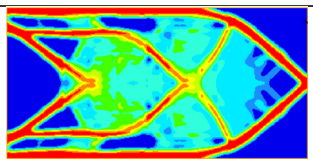 | 146 | 27.0 | 30.8 |
| 10 | 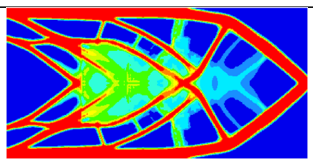 | 143 | 55.0 | 62.2 |

It is important to note that some topologies representing the same design concept can receive different scores depending on the mathematical formulation of the interpretability (DI) and stiffness scores. In this case, results 4 and 7 illustrate the same structural design. However, result 4 exhibits a more defined density distribution (with primarily red and blue regions), which leads to a higher stiffness score (83.6% compared to 77.4%) and a higher DI (98.0% compared to 74.0%). The same principle applies to results 5 and 8. These findings will be discussed in more details in the next Section.

## 3.6 Analysis of the Resulting Topologies and Corresponding Performance Indicators

Results 2, 4, and 5 exhibit the highest DI scores, while solution 3 achieves the highest stiffness score as seen in Table 3.4. Result 2, with a DP of 2 (greater than 1), further penalizes intermediate densities, which leads to the emergence of a checkerboard pattern. This pattern artificially increases both stiffness and DI, indicating a potential issue in the optimization process. The MINDIM constraint helps to avoid the checkerboard pattern in the final result.

Although the overall quality of the result can be debated, a clear trend emerges: solutions tend to show higher DI values when the stiffness score is also high, suggesting a correlation between these metrics, as we can see in Figure 3.6.

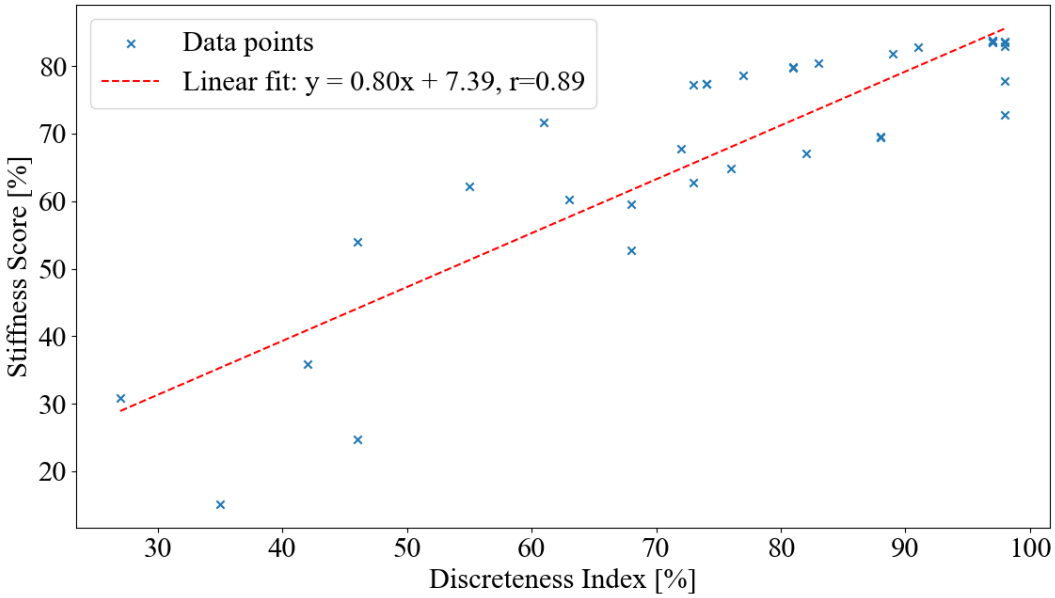


Figure 3.6 Correlation between DI and Stiffness Score for the Cantilever beam

Based on this correlation, it is evident that regardless of whether the Compliance Score (Stiffness) or DI (Interpretability/Manufacturability) is prioritized, both lead in the same direction. The optimal solution could be found by defining a total score.

$$\text{Total Score}[\%] = w_{DI} \times \text{DI}[\%] + w_{Stiffness} \times \text{Stiffness Score}[\%]$$

where $w_{DI}$ represents the significance associated with interpretability, while $w_{Stiffness}$ denotes the importance related to structural aspects. Depending on the industry and engineering requirements, both weights may be adjusted. Table 3.5 presents a ranking of precedents

results assuming both scores are equally important ($w_{DI} = w_{Stiffness} = \frac{1}{2}$).

Table 3.5 Ranking of the TO results based on a combination of DI and stiffness score. Red pixels indicate the highest density value of 1, blue pixels correspond to the lowest density value of 0, and intermediate colors represent values between these two extremes

| Rank | Result No. | Result Image | DI [%] | Stiffness Score [%] | Total Score [%] |
|---|---|---|---|---|---|
| 1 | 4 | 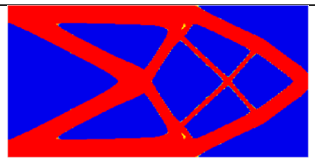 | 98.0 | 83.6 | **90.8** |
| 2 | 5 | 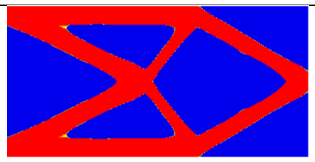 | 98.0 | 83.5 | **90.8** |
| 3 | 3 | 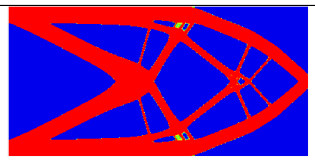 | 98.0 | 82.9 | **90.5** |
| 4 | 2 | 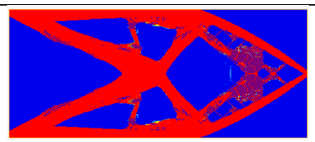 | 98.0 | 77.8 | **87.9** |
| 5 | 1 | 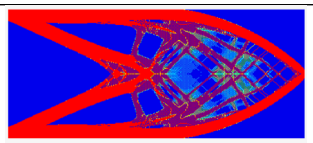 | 91.0 | 82.8 | **86.9** |
| 6 | 7 | 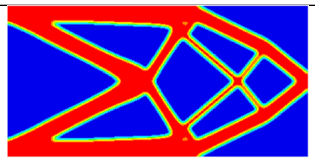 | 74.0 | 77.4 | **75.2** |
| 7 | 8 | 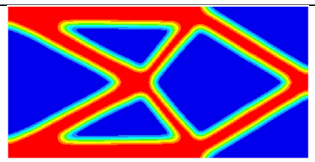 | 61.0 | 71.6 | **66.8** |
| 8 | 10 | 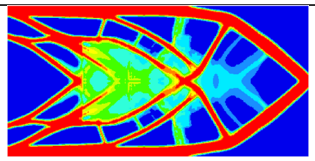 | 55.0 | 62.2 | **58.6** |

| Rank | Result No. | Result Image | DI [%] | Stiffness Score [%] | Total Score [%] |
|---|---|---|---|---|---|
| 9 | 9 | 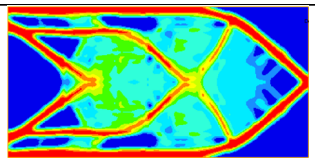 | 27.0 | 30.8 | **28.9** |
| 10 | 6 | 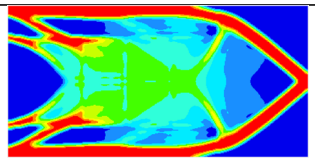 | 35.0 | 15.1 | **25.1** |

Solutions that receive high scores are considered advantageous candidates in the context of structural TO. This scoring metric facilitates the decision-making process by offering a more objective foundation for selecting designs, thereby reducing reliance solely on engineering intuition. Based on this preliminary evaluation, results 4 and 5 emerge as the most promising alternatives. Although some solutions, such as results 4 and 7 or results 5 and 8, represent variations of the same underlying design concept, the objective of identifying the most favorable design is nonetheless achieved. The performance metric effectively captures subtle differences between these design variations, correctly identifying that result 4 outperforms result 7. Although result 7 is an altered version of result 4, it lacks the clear delimitation between essential load-carrying membranes and regions of the design space that can remain unused. The same explanation applies to result 8, which is an altered version of result 5 with a lower gradient of density at the edges of the design concept.

### 3.7 Validation of the Performance Indicator

The performance metric was assessed by comparing it to the intuition and experience of five experts in density based TO. An expert was defined as either a PhD holder in the TO field or someone with over one year of experience using TO algorithms. A survey was distributed, presenting the resulting topologies in a randomized order. The TO results were shown as density plots without any metric information to avoid bias. Respondents were unaware of each other's responses, ensuring an independent evaluation process. The experts were asked to rank them based on their design expertise, considering the boundary conditions illustrated in Figure 3.1. This method of validation, similar in nature to a blind consensus-free expert ranking, allowed for a quantitative comparison between subjective expert opinion and the objective metric-based ranking, providing a measure of alignment between perceived design quality and the proposed scoring system. The top three and bottom three results were ranked

in the exact order predicted by the performance metric. While individual experts exhibited slight variations in their rankings of each topology, the averaged expert rankings aligned with the performance metric's ordering. This slight variation in expert opinions, based on an educated assessment of overall result quality, highlights the importance of an absolute quantitative score for a more objective evaluation.

Integrating quantitative performance metrics is essential in high-precision industries like aerospace, where stringent constraints on weight, manufacturability, and structural integrity must be met. Relying solely on engineering intuition can lead to suboptimal choices, whereas data-driven decision-making ensures that TO results align more reliably with design requirements and performance objectives.

### 3.8 Structural Pattern Recognition

After generating multiple TO results based on input constraints, we obtain a range of design variations as we saw in Section 3.5. In some cases, the optimal and most feasible design may be a combination of several results. By averaging the top-performing TO results based on a performance metric, we can generate a density-based image that reveals common structural features across different design outcomes. Each CQUAD4 element from the FEM can be related to a pixel in an image. Suppose that we have $n$ TO results, and we are interested in observing a pattern among them. To do this, we can apply a grayscale filter and calculate an average density at each pixel location $(i, j)$ across all TO results. Let $\rho_{TO_k}(i, j)$ represent the density distribution in the $k^{\text{th}}$ TO result. The average density $\bar{\rho}(i, j)$ at position $(i, j)$ can then be computed as:

$$\bar{\rho}(i, j) = \frac{1}{n} \sum_{k=1}^{n} \rho_{TO_k}(i, j) \tag{3.7}$$

This matrix $\bar{\rho}(i, j)$ represents the average density in all selected TO results from different inputs parameters, providing a single image that indicates common structural patterns as illustrated in Figure 3.7.

Before averaging the density across multiple TO results, it is essential to align the images to a common scale, as they may vary in pixel dimensions. A preliminary step is to identify the contour of the regions to be superposed, ensuring proper scaling of all images before overlaying them.

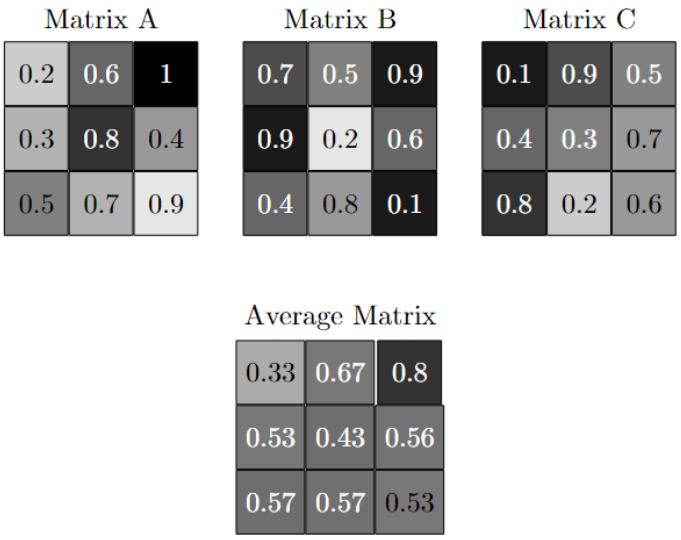


Figure 3.7 Visualization of an averaged density image derived from three TO results, represented as a simplified $3 \times 3$ grid of images

By selecting results 3, 4, and 5 from Section 3.5, chosen for their high scores based on the metrics defined in Section 3.4, we can observe a structural pattern across the TO results. This pattern becomes clearer with superposition: pixels with a density of 1 (fully black) indicate that a structural membrane appears in that pixel location in all selected TO results, while pixels with a density of 0 (fully white) indicate that no structural membrane is present in any of the results, as shown in Figure 3.8.

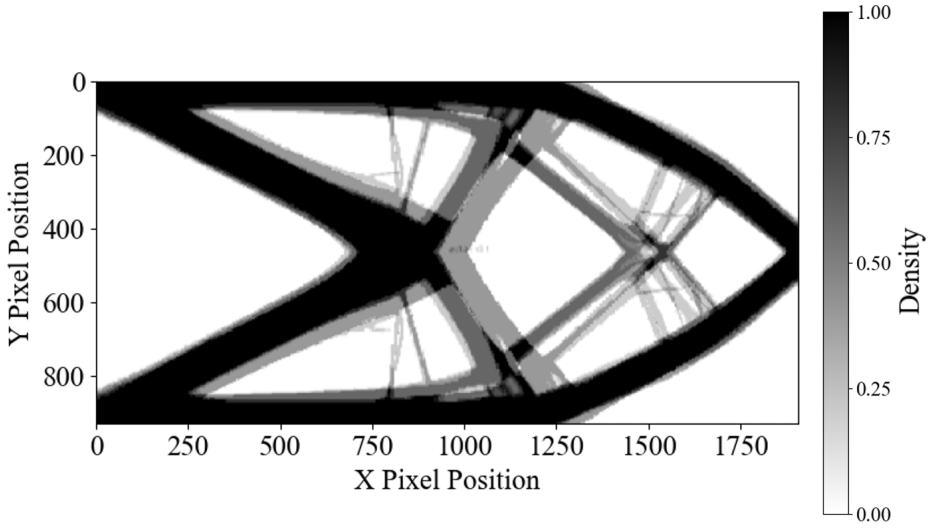


Figure 3.8 Superposition of the density distributions obtained from TO results for cantilever 3,4 and 5, illustrating the combined material layout and structural patterns emerging across different optimization scenarios.

Distinct membrane patterns appear at the force application point on the cantilever beam and at the support points in the truss configuration across all three results. For instance, a clear pattern emerges at the support located at the bottom and top left, where the area inside the truss support remains hollow. Additionally, smaller membrane features, shown in grey, are visible near the force application point. However, these features are less distinct since they appear in only one or two TO results. This overlay helps identify the structural regions that should be prioritized for further refinement of the final design. Result 5 shares the most similarities with the final design from Figure 3.8, as it incorporates the main load paths observed in results 3 and 4.

In this approach, we consider the superposition of multiple TO results for a single load case. However, it is also possible to perform TO for multiple distinct load cases on the same design space and superimpose the results. This enables the identification of common loadpath within the design space that are critical across various loading scenarios. The TO results for each load case can be selected based on a consistent performance metric, using both stiffness and interpretability as key evaluation criteria.

A practical and meaningful way to combine these results is by computing a weighted density field, where each load case is assigned a weight according to its relative criticality. The superposition is then performed using these weights.

Let $\rho_{LC_k}(i,j)$ denote the density distribution resulting from the $k^{\text{th}}$ load case, and let $w_k$ be the corresponding weight.

If the weights are normalized such that:

$$\sum_{k=1}^{n} w_k = 1 \tag{3.8}$$

then the final density distribution $\rho_{\text{final}}(i,j)$ is given by:

$$\rho_{\text{final}}(i,j) = \sum_{k=1}^{n} w_k \cdot \rho_{LC_k}(i,j) \tag{3.9}$$

While the weighted superposition of TO results for multiple load cases provides a valuable means of identifying shared structural features and common load paths, it must be applied with caution. The resulting density field, derived from independently optimized solutions, may not correspond to a physically realizable or mechanically optimal structure under any individual load case. In particular, the superposition may introduce intermediate density regions that are neither structurally meaningful nor manufacturable, and may highlight areas

that are not truly critical under any single scenario, especially if the assigned weights do not accurately reflect the relative importance of each load case. As such, this method should be used primarily as a tool for design interpretation or concept generation, rather than as a substitute for a full multi-load-case optimization. Its main strength lies in revealing recurrent load paths and guiding the placement of structural reinforcements in a balanced manner. To ensure meaningful results, TO outputs should be selected using consistent performance metrics, and weights must be carefully normalized to reflect the actual criticality of each load case within the overall design context.

## 3.9 Conclusion

In summary, the implementation of a scoring system in TO can provide structural engineers with a valuable tool to objectively evaluate design performance using quantitative criteria. The methodology presented in this chapter, applied to a simplified case, lays the foundation for its application in more complex scenarios. In Chapter 4, this same approach will be extended to a higher level of system complexity : the BWB. The underlying working hypothesis, a scalability hypothesis, is that the design strategy validated in the current Chapter will remain effective and yield meaningful results when scaled to the full complexity of the system.

# CHAPTER 4 TOPOLOGY OPTIMIZATION FRAMEWORK APPLIED TO THE BLENDED WING BODY AIRCRAFT

This section applies the methodology outlined in Chapter 3 to the BWB aircraft by integrating multiple load cases into the TO boundary conditions to simulate aerodynamic forces. The resulting analysis offers insights into the load paths generated by each aerodynamic load case and supports the identification of an optimal stiffener distribution. These outcomes directly address SO2: Determine the optimal stiffener layout of a BWB using TO results under multiple loading scenarios. Finally, the chapter concludes with an assessment of SO3: Develop a visual guideline for the execution of the developed framework.

## 4.1 Geometric and Finite Element Models

### 4.1.1 Computer Aided Design Geometry of the Blended Wing Body

A 2D surface model is preferred to guide the TO algorithm in achieving an optimal density distribution at the skin level as seen in [32] and [33]. This approach is also less computationally intensive compared to using 3D elements such as tetrahedral and hexahedral elements. The IGES files contain multiple surfaces that represent the geometry of the aircraft's outer skin, modeled using a custom NACA 4317 airfoil profile as shown in Figure 4.1 and 4.2.

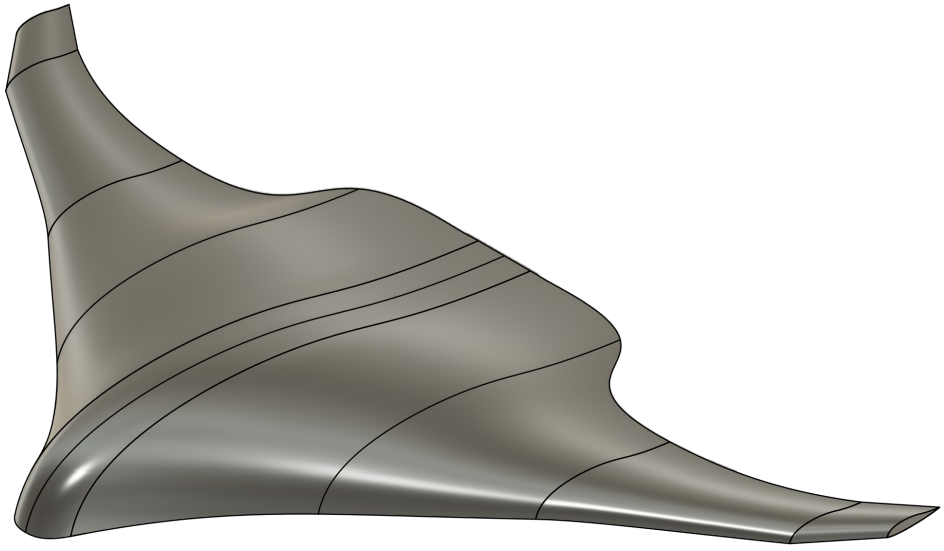

Figure 4.1 Aerodynamic skin of the BWB aircraft based on custom NACA 4317 airfoil profile

This self-designed model allows for quick modifications to dimensions or the addition of specific curves, facilitating FEM analysis. The FEM model is parametric, meaning the aerodynamic loads acting on it are influenced by its dimensions and mass. As long as the proportions remain consistent, the specific dimensions are irrelevant and the results will be the same. The BWB miniature model has a length of 550 mm, a total wingspan of 1000 mm, and a height of 92 mm.

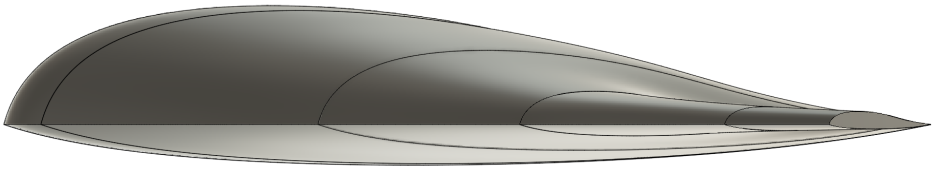

Figure 4.2 Side view of the skin of the BWB aircraft based on custom NACA 4317 profile

### 4.1.2 Finite Element Models Overview

In this TO study, the boundary conditions have been deliberately simplified to facilitate the understanding of load paths throughout the aircraft structure during take-off (Upbending), landing, roll maneuvers, and engine thrust. The emphasis is on the fundamental mechanics involved, rather than on achieving high precision in the model, as TO remains in the preliminary design phase. It is important to note that the pressurization load case should be considered for an optimal design, although it was not addressed in this study, as it lies beyond the scope of this master's work. To optimize computational efficiency, the FEM model represents one-half of the CAD model, utilizing symmetry and anti-symmetry to simulate the specified load case. To fully constrain rigid body motion without introducing excessive stiffness, a method similar to the 3-2-1 constraint approach is applied. In this system, constraints 1, 2, and 3 correspond to translations in the model's coordinate system, while constraints 4, 5, and 6 govern rotations about axes 1, 2, and 3. The symmetry plane restricts out-of-plane motion (1, 5, 6), whereas anti-symmetry constrains in-plane motion (2, 3, 4). Table 4.1 shows how the half model was constrained for the subsequent TO.

Table 4.1 Load case overview for subsequent BWB TO. Green triangle shows the position of each SPCs with the respective DOF blocked. The force and moment location/orientation are shown in red with single arrow and double arrow respectively. The green hatched zone present the geometry symmetry while de red hatched zone presents the anti-symmetry

| Load Case | Symmetry or Anti-symmetry | Isometric View | Bottom View |
|---|---|---|---|
| Upbending | Symmetry | 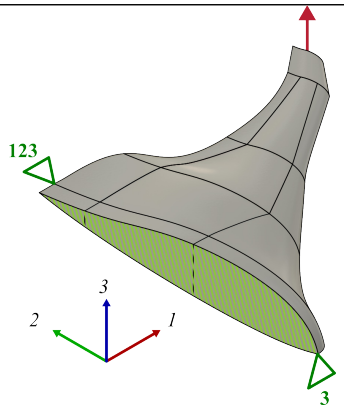  | 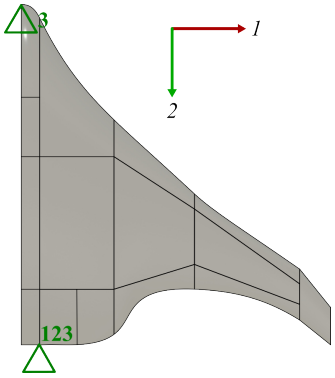  |
| Landing | Symmetry | 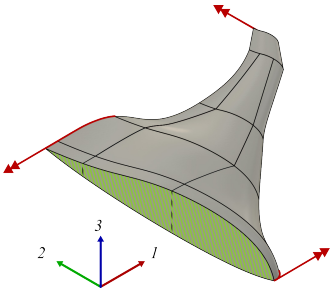  | 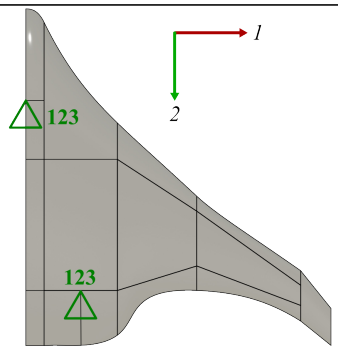  |
| Roll | Anti-Symmetry | 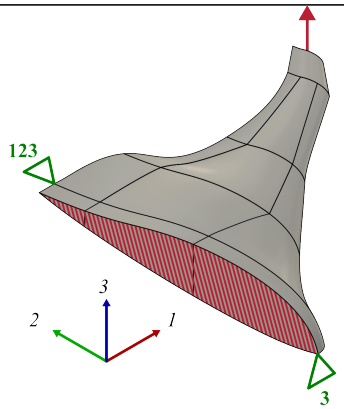  | 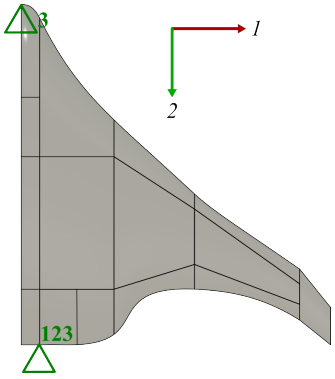  |

| Load Case | Symmetry or Anti-symmetry | Isometric View | Bottom View |
|---|---|---|---|
| Engine Thrust | Symmetry | 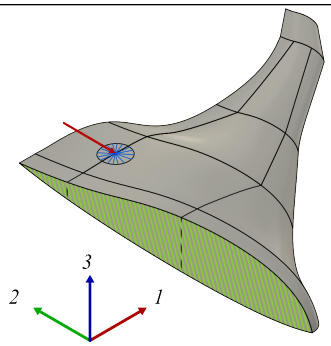  | 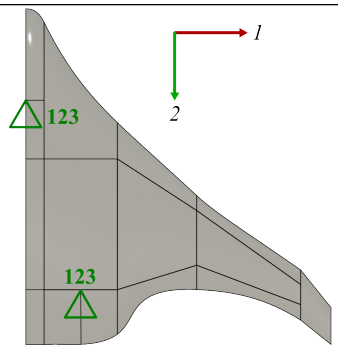  |

The rationale for the boundary conditions is explained in greater detail in each section for the specified load case. Table 4.1 can help to understand how each model was constraint for the subsequent mesh convergence analysis.

## 4.2 Mesh Convergence Analysis

To ensure consistency in the analysis and results, a common mesh size will be selected for all load cases. All FEM models will follow the same convergence analysis, with compliance as the key parameter, as outlined in Chapter 3. For design and resolution purposes, the finest membrane element should be at least 0.5% of the total wingspan. This translates to a maximum mesh size of 1.67 mm and it's related to the MINDIM constraint as explained in Section 3. However, the mesh must still converge for all FEM models. The mesh sizes used for the convergence analysis are 16 mm, 14 mm, 8 mm, 4 mm, 2 mm, 1 mm, and 0.5 mm, as shown in Figure 4.3. The relative compliance $C^*$ is normalized using the maximum compliance of each load case.

For the outer skin FEM model , a mesh size of 1 mm (267,997 elements) is sufficient for the analysis, as reducing it to 0.5 mm results in an average relative compliance change of just 0.51%, while increasing CPU time by approximately 264%. The simulations were run on a computer equipped with an Intel Core i7-6700K processor (4 GHz), 64 GB of RAM, and an NVIDIA GeForce GTX 1080 Ti graphics card.

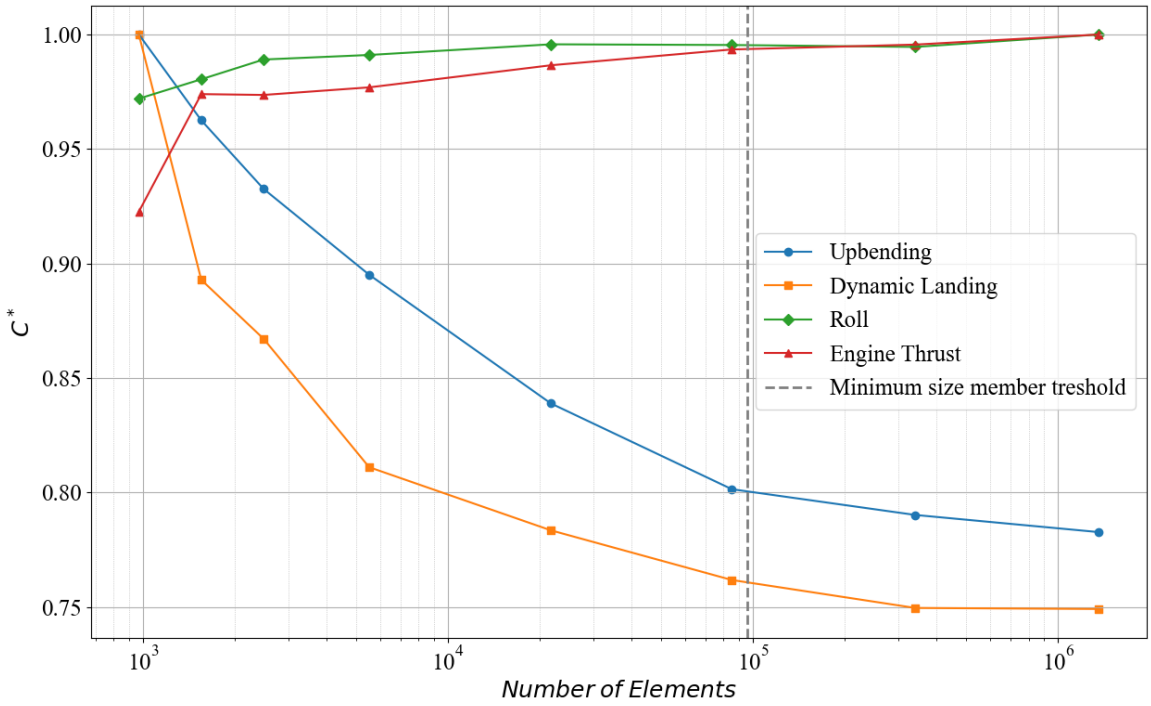


Figure 4.3 Relative compliance of the TO BWB stiffened shell structure for each load case

For all subsequent TO, parameters from Table 4.2 are constrained to guarantee a converged optimization.

Table 4.2 Fixed parameters for subsequent BWB TO

| | |
|---|---|
| **Global Mesh size** | 1 mm |
| **Element Type** | CQUAD4,CTRIA3 |
| **Constraint** | $V(\rho) \leq V_{\max} = 0.4$ |
| **Objective** | min(Compliance) |
| **Maximum iteration** | 200 |
| **OBJTOL** | 0.001 |

## 4.3 Topology Optimization | Upbending Load Case

In this analysis, the boundary conditions for the Upbending load case have been implemented with the aim of simulating the aircraft's behavior under lift-off conditions while avoiding unnecessary stiffening of the model.

### 4.3.1 Finite Element Model and Boundary Conditions

The aircraft is supported at two nodes located near its center as seen in Table 4.1, with a symmetry constraint applied to fully restrict rigid body motion. To simulate upward bending during take-off, a force equal to half the aircraft weight is applied at each wingtip through Rigid Body Element (RBE3) connections as an approximation. The location at the wing tip for the force helps in identifying the loadpath through the entire wing. It is important to highlight that the magnitude of the applied forces is not significant when compliance is used as the objective function in the optimization process. This force replicates the bending moment experienced by the wings during takeoff.

Although this setup does not perfectly represent take-off dynamics, it adequately satisfies the take-off boundary conditions for a TO analysis. The use of vertical forces instead of a pressure distribution is justified, as PLOAD4 applied to 2D shell elements often leads to inaccurate TO results. Moreover, this load case, which is defined by applied forces, represents the most conservative scenario, as the load is applied entirely at the wing tips, far from the supported nodes. This configuration ensures that the structural response captures the maximum possible loading effect.

The optimal input parameters for all TO load cases are provided in Table 4.3. As shown in Appendix A, which presents all the optimizations performed in this study, setting MINDIM to three times the mesh size while omitting MAXDIM consistently yields the best optimization results. This configuration introduces an additional constraint that promotes the formation of fully developed load-bearing membranes without overly restricting the optimization process, thereby facilitating convergence toward an optimal solution with both high stiffness score and interpretability.

Table 4.3 Best TO inputs for all load cases

| | |
|---|---|
| **MINDIM** | $3h$ |
| **MAXDIM** | N/A |
| **DP** | 1 |
| **APPLIED TO** | ALL |

### 4.3.2 Upbending Results | Stiffened Shell Model

As shown in Figure 4.4, a unique stiffening pattern emerges on the aircraft skin. At the wing's leading edge, a substantial membrane structure forms, efficiently channeling the load path to the fuselage through a combination of thick and narrow membrane regions for both the top and bottom structure. The TO leverages the double curvature between the upper and

lower skins, enhancing rigidity through out-of-plane stresses. Vertical membranes positioned at the fuselage center provide resistance to bending in that region. The TO maximizes the use of the available design space to stiffen the aircraft in the wing upbending load case and gives the outputs metrics represented in Table 4.4.

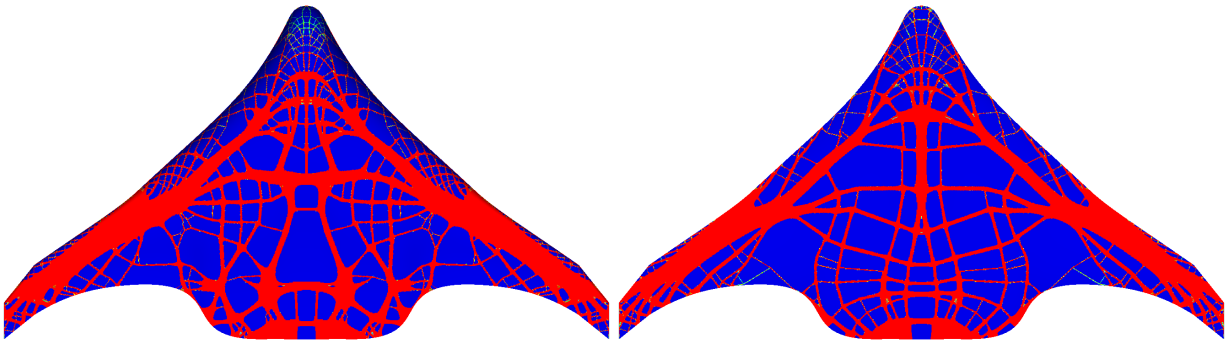

(a) Top view (b) Bottom view

Figure 4.4 Optimal density distribution results of the stiffened shell structure of the BWB under the upbending load case: (a) Top View, (b) Bottom View

Table 4.4 TO metrics | Stiffened shell structure | Upbending

| | |
|---|---|
| **Number of iterations** | 97 |
| **Mass [kg]** | 0.286 |
| **Compliance [Nmm]** | 2.17 |
| **DI [%]** | 96.0 |
| **STIFFNESS SCORE [%]** | 79.7 |
| **TOTAL SCORE [%]** | 87.9 |

As a reminder, the compliance-based stiffness score is computed using:

$$\text{Stiffness Score } [\%] = \left(1 - \frac{C - C_{\min}}{C_{\max} - C_{\min}}\right) \times 100 \tag{4.1}$$

where $C$ represents the absolute compliance at the end of the optimization process for a given volume fraction. $C_{\min}$ corresponds to the maximum achievable stiffness within the design space, while $C_{\max}$ represents the minimum stiffness obtained for the same volume fraction.

The DI is defined as:

$$\text{DI } [\%] = \frac{\sum_{e=1}^{n} \rho_e V_e \quad \text{if} \quad 0.9 \leq \rho_e \leq 1.0}{\sum_{e=1}^{n} \rho_e V_e} \times 100 \tag{4.2}$$

where $\rho_e$ and $V_e$ are the density and volume of element $e$, respectively.

The final score is computed as a weighted combination of the two metrics :

$$\text{Total Score } [\%] = w_{\text{DI}} \times \text{DI } [\%] + w_{\text{Stiffness}} \times \text{Stiffness Score } [\%] \tag{4.3}$$

The weight of each metric is set to $\frac{1}{2}$, as stiffness and interpretability are considered to be equally important in this study.

As shown in Table A.1 in Appendix A, the results vary significantly depending on the input parameters. Among them, the configuration illustrated in Figure 4.4 achieves the best overall performance, with a DI of 96.0% and a stiffness score of 79.7%. Although the stiffness is slightly lower than the result obtained without the MINDIM constraint (80.5%), this is expected due to the less restrictive nature of the unconstrained optimization. Furthermore, the addition of the MINDIM constraint effectively eliminates the checkerboard pattern from the optimization with no size member constraint.

The optimal topology was used to manufacture a 3D stiffened shell structure for demonstration purposes. Although the methodology used to extract the stiffeners from the 2D shell of the TO result falls outside the scope of this thesis, it is nonetheless explained in Appendix B.

## 4.4 Topology Optimization | Dynamic Landing Load Case

In this analysis, the boundary conditions for the Dynamic Landing load case have been established to simulate the aircraft structure behavior during landing while maintaining a focus on identifying critical load paths.

### 4.4.1 Finite Element Model and Boundary Conditions

The landing gear has been constrained at all six degrees of freedom (DOF), fixing it in position at three different points (with symmetry), as seen in Table 4.1. Moments have been applied to the wings and the upper and lower sections of the fuselage with RBE3 connections to simulate the bending forces due to the vertical deceleration during landing. These moments are proportional to the length and weight of the wing/fuselage structure relative to the nearest fixed point.

### 4.4.2 Dynamic Landing Results | Stiffened Shell Model

As illustrated in Figure 4.5, the optimized topology features a large membrane at the wingtip, where moments are applied to the RBE3 connection. This prominent wing membrane is then split in half, connecting to the rear and front landing gear. Similar to the Upbending load case, the structure utilizes the double curvature to reinforce the design, with small membrane formations arranged in circular patterns. The RBE3 connection at the fuselage's rear, where a moment is applied, forms a substantial, rigid area that directly links to the rear landing gear. Additionally, the optimization suggests the presence of structural elements at the wing's leading edge, an area where the aileron would typically be located, posing a potential issue.

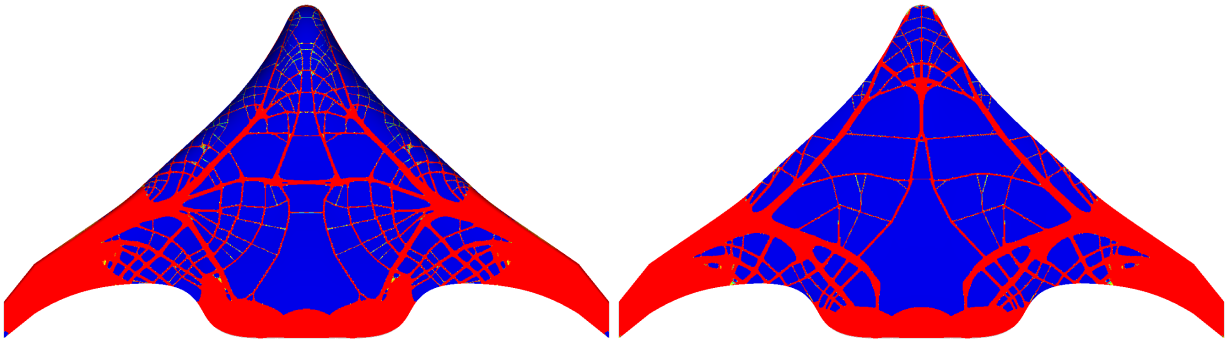

(a) Top view (b) Bottom view

Figure 4.5 Optimal density distribution results of the stiffened shell structure of the BWB under the dynamic landing load case: (a) Top View, (b) Bottom View

Table 4.5 TO metrics | Stiffened shell structure | Dynamic Landing

| | |
|---|---|
| **Number of iterations** | 84 |
| **Mass [kg]** | 0.286 |
| **Compliance [Nmm]** | 0.97 |
| **DI [%]** | 96.0 |
| **STIFFNESS SCORE [%]** | 94.5 |
| **TOTAL SCORE [%]** | 95.2 |

As detailed in Table A.2 in Appendix A, the optimization results exhibit considerable sensitivity to the choice of input parameters. The configuration presented in Figure 4.5 stands out for its overall effectiveness, achieving a DI of 96.0% and a stiffness score of 94.5%. Although this stiffness value is marginally lower than the 94.6% obtained from the unconstrained case, the difference is consistent with expectations, as the absence of a minimum member size MINDIM constraint allows for a more flexible but less realistic design. Importantly, in-

troducing the MINDIM constraint successfully removes the checkerboard pattern typically observed in unconstrained topologies.

The impact of constraints is further highlighted by the inclusion of a MAXDIM parameter, which significantly influences the convergence behavior of the optimization under landing conditions. A lot of optimization with the MAXDIM constraint had compliance higher that the initial compliance, which resulted in stiffness score of 0%, based on our metric definition. Additionally, the structural topologies generated with the MINDIM constraint consistently emphasize the role of the wings, which are reinforced through a triangular membrane that links them to both the front and rear landing gears.

## 4.5 Topology Optimization | Roll Load Case

In this analysis, the torsion load case has been designed to simulate the structural behavior of the aircraft under asymmetric loading conditions that induce twisting moments about the longitudinal axis of the BWB. This load case complements other load cases, such as the Upbending and Dynamic Landing, by addressing unique stress environments such as differential wing forces or yaw-induced torsion.

### 4.5.1 Finite Element Model and Boundary Conditions

The torsion load case is similar to the Upbending load case, as both use the same single-point constraints at three identical locations, ensuring consistency in the boundary conditions. However, instead of a symmetry constraint, an asymmetry constraint is applied to the model, reversing the vertical force at the opposite wingtip, simulating an inertial effect during a roll maneuver.

### 4.5.2 Roll Results | Stiffened Shell Model

As shown in Figure 4.6, the result differs from the Upbending load case due to the anti symmetry constraint. In this case, the algorithm cannot treat the symmetry plane as a rigid surface, as rotation of the symmetry plane is allowed. This enables membranes to form in a cross pattern at the fuselage center. Similarly to the Upbending case, the roll optimization heavily utilizes the wing's leading edge, where a traditional structure would typically feature a spar. This large structure is then divided into smaller membranes that connect to a rigid structure at the rear fuselage. The bottom of the front fuselage remains unstiffened, as the load path is mainly concentrated and distributed toward the rear of the aircraft.

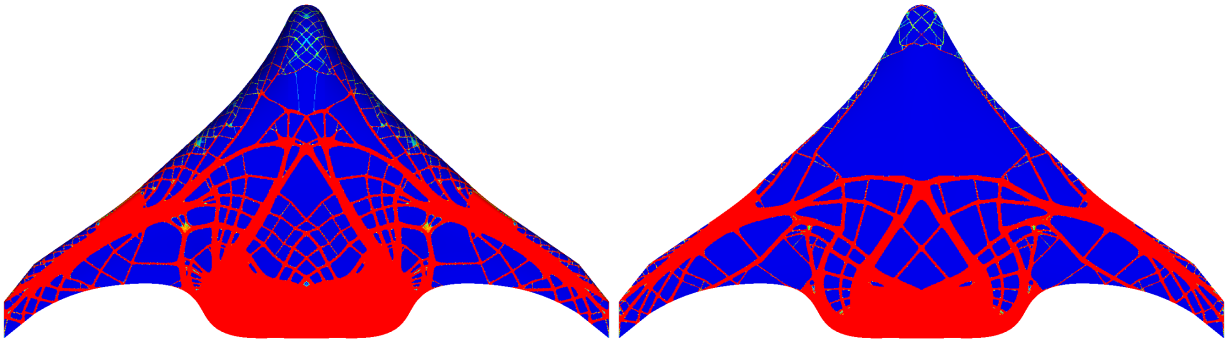

(a) Top view (b) Bottom view

Figure 4.6 Optimal density distribution results of the stiffened shell structure of the BWB under the Roll load case: (a) Top View, (b) Bottom View

Table 4.6 TO metrics | Stiffened shell structure | Roll

| | |
|---|---|
| **Number of iterations** | 74 |
| **Mass [kg]** | 0.286 |
| **Compliance [Nmm]** | 13.11 |
| **DI [%]** | 95.0 |
| **STIFFNESS SCORE [%]** | 96.4 |
| **TOTAL SCORE [%]** | 95.7 |

As shown in Table A.3 in Appendix A, the results vary significantly depending on the input parameters. The configuration illustrated in Figure 4.6 achieves the best overall performance, with a DI of 95.0% and a stiffness score of 96.4%. All MINDIM only optimizations share common characteristics and differ only slightly in terms of topology and performance scores.

The presence of the MINDIM constraint helps reveal load paths that remain unclear in the unconstrained TO results. In unconstrained cases, small load paths between larger structural elements often fail to converge properly, making it difficult to interpret the structural behavior. The MINDIM constraint plays a key role in promoting well-defined and interpretable paths for load transfer.

## 4.6 Topology Optimization | Engine Thrust Load Case

In this analysis, we aim to determine the most optimal structure for the engine mounted at the rear top of the fuselage. We simulate the effects of the engine while the aircraft is on the ground, ready for takeoff.

### 4.6.1 Finite Element Model and Boundary Conditions

The structural response of the engine thrust is simulated by applying a horizontal force to the RBE3 at the rear of the fuselage, where the engine could be located. The front and rear landing gear are assumed to be infinitely rigid, representing the contact with the ground during take-off.

### 4.6.2 Engine Thrust Results | Stiffened Shell Model

As shown in Figure 4.7, the wings are not stiffened in the case of engine loading, which is expected. The path of the load extends from the location of the engine mount, with thick membranes that direct the load to the front and rear landing gear. The landing gear areas are also heavily reinforced, as the load path is directly transferred to them. In addition, the algorithm makes extensive use of the junction between the top and bottom fuselage to distribute the load, with the curvature helping to stiffen the structure.

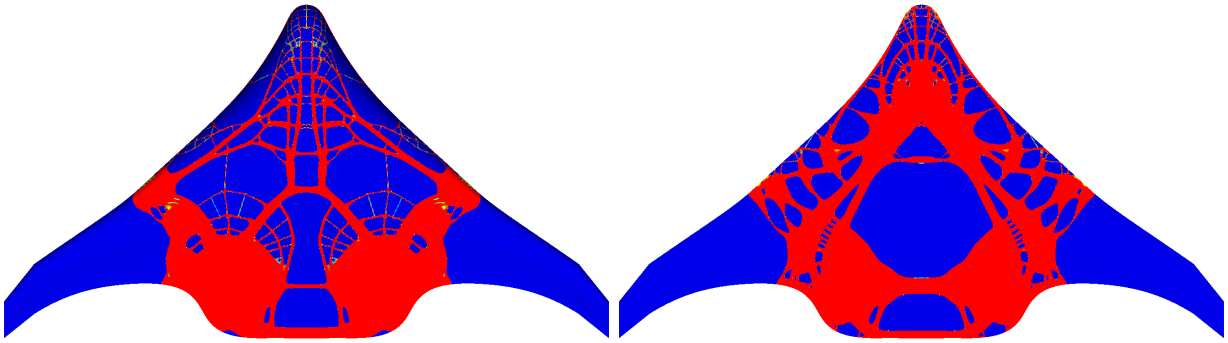

(a) Top view (b) Bottom view

Figure 4.7 Optimal density distribution results of the stiffened shell structure of the BWB under the Engine Thrust load case: (a) Top View, (b) Bottom View

Table 4.7 TO metrics | Stiffened shell structure | Engine Thrust

| | |
|---|---|
| **Number of iterations** | 67 |
| **Mass [kg]** | 0.286 |
| **Compliance [Nmm]** | 9.58 |
| **DI [%]** | 91.5 |
| **STIFFNESS SCORE [%]** | 97.0 |
| **TOTAL SCORE [%]** | 94.3 |

As shown in Table A.4 in Appendix A, the results exhibit significant variability depending on the input parameters. The configuration displayed in Figure 4.7 delivers the best overall

performance, with a DI of 91.5% and a stiffness score of 97.0%, yielding a total score of 94.3%.

In this load case, the MAXDIM constraint also greatly affects convergence behavior like the landing load case. Increasing the MAXDIM value, thereby making the optimization less restrictive, tends to reduce both the stiffness and interpretability of certain results. These findings support the conclusion that the MINDIM constraint consistently improves the quality of the solutions across all load cases considered in this study, whereas the MAXDIM constraint systematically introduces significant alterations to the resulting topologies.

## 4.7 Combined Load Case Analysis for the Stiffened Shell Structure of the Blended Wing Body

To identify structural patterns emerging from different load cases, the best result based on the TO metric from each load case can be superimposed, assuming equal weighting. This assumption is made due to the lack of access to actual aircraft weight distributions corresponding to the load cases. In the absence of industrial data specifying the relative criticality of each load case, all four are considered to have equal importance. The superposition is done using 8-bit greyscale images of the TO results. The intensity of each pixel ranges from 0, representing black, to 255, representing white.

Figure 4.8 presents the superposition obtained from the upbending, landing, roll, and engine load cases shown in Figures 4.4, 4.5, 4.6, and 4.7. The predominant load path originates from the wingtip, distributing loads toward the front of the wing, while significant structural reinforcements appear at the engine location, forming distinct thick black members.

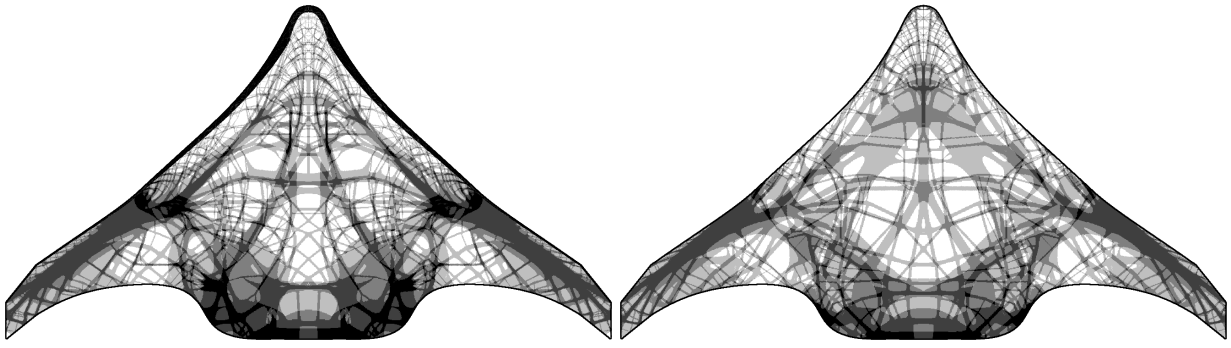

(a) Top view (b) Bottom view

Figure 4.8 Superposition of the optimal topology obtained for the stiffened shell structure under upbending, landing, roll, and engine thrust load cases. Black regions indicate areas that appear in all load cases, while white regions correspond to areas that are never selected

To identify the critical membranes in the superimposed optimal topology, an image thresholding technique can be applied. This approach aids the designer in detecting the primary load paths by filtering out the less significant grey areas resulting from the superposition. As a result, it becomes possible to extract a structural skeleton that can be observed from multiple perspectives. Figure 4.9 illustrates this concept using a 8-bit binary greyscale threshold of 190 effectively removing the lighter grey regions.

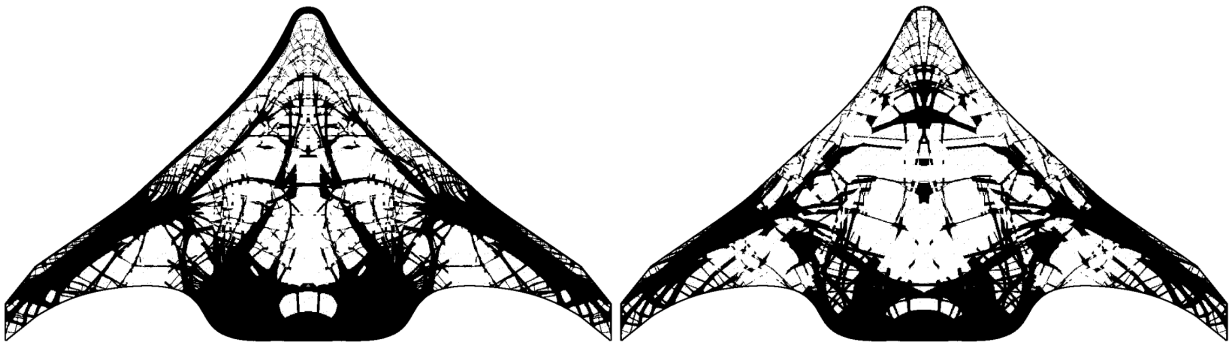

(a) Top view (b) Bottom view

Figure 4.9 Binary threshold of 190 for the superposition of all load cases

Figure 4.9 shows that the dominant load paths originate from the wings and converge at the fuselage center through a triangular pattern on top and horizontal connections at the bottom—highlighting a key structural feature of the BWB configuration. However, the thresholding process broke several membranes that were previously continuous in the superimposed topology. Adjusting the threshold may help restore connectivity. Alternatively, if the goal is to highlight less common load paths shown in grey, a higher binary threshold can be used to convert these regions to black, as shown in Figure 4.10.

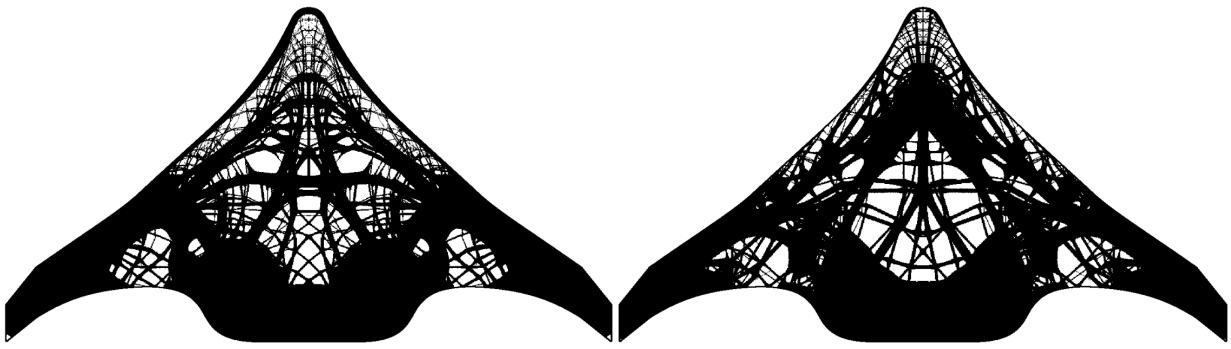

(a) Top view (b) Bottom view

Figure 4.10 Binary threshold of 200 for the superposition of all load cases

A clearly visible non-loaded region (white zone) emerges from the visualization. This can assist in identifying areas that do not require structural reinforcement, thereby guiding systems engineers in placing aircraft subsystems that are not structurally critical. The saturated view also highlights numerous black regions, indicating that the load paths vary significantly across different load cases, each activating distinct portions of the structure.

## 4.8 Visual Guideline for the execution of the developed framework

As part of this research, sub-objective 3 (SO3) was to finalize the developed framework and produce a comprehensive visual diagram that summarizes the overall methodology.

It was possible to highlight the structural load paths for multiple load cases on the BWB structure by using an in-house developed metric presented in Chapter 3, combined with image-based post-processing algorithms. Figure 4.11 provides a visual guideline for the execution of the framework developed and used in the current chapter. The process begins by selecting the best TO result for each individual load case, achieved by adjusting TO input parameters and choosing appropriate values for $w_{DI}$ and $w_{stiffness}$. Stiffness and interpretability were considered equally important criteria in the selection of the optimal TO result in this study. The optimal TO results are subsequently combined using specific weights, $w_{LC_1}, w_{LC_k}, \ldots, w_{LC_N}$, which reflect the criticality of each load case. In this study, all load case weights were assumed to be equal due to the lack of industrial data specifying their relative importance.

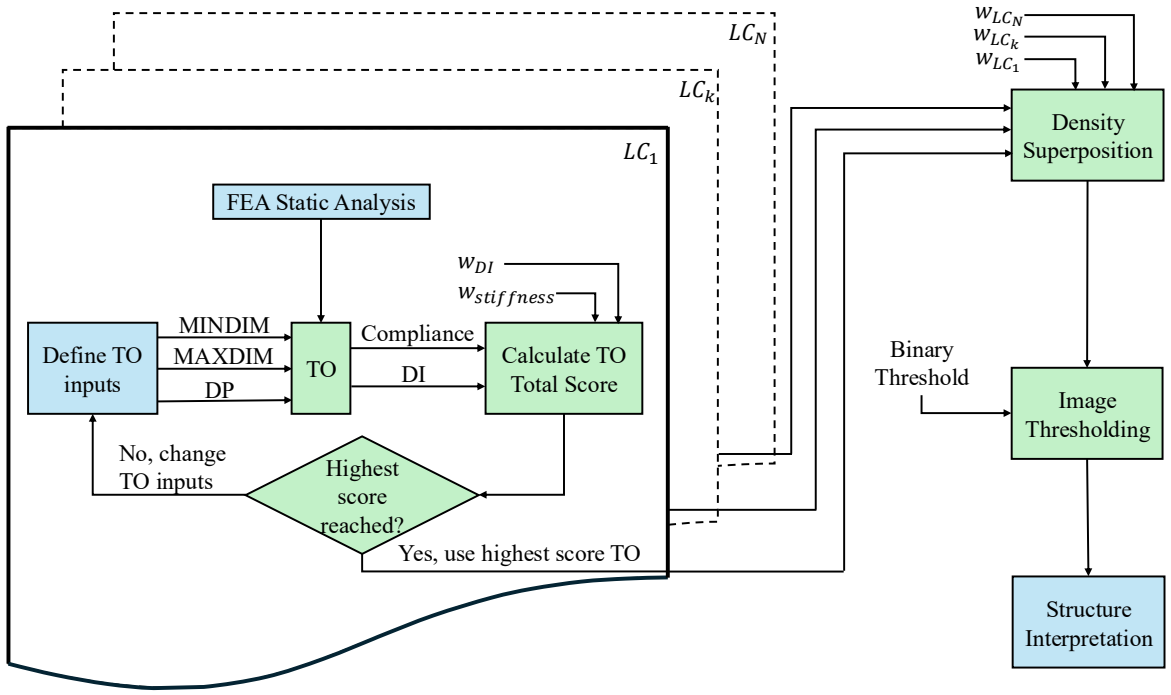


Figure 4.11 Visual guideline for the execution of the developed framework designed to help structural engineers identify critical load paths when using multiple TO results under $N$ load cases (LCs). Blue-filled shapes represent actions taken by the structural engineer, while green-filled shapes indicate automated actions performed by the algorithm discussed in this Master's

The use of visual algorithms with TO proves to be valuable during the early stages of the design process by identifying critical load paths of the structure. However, the absence of a closed FEA loop, where the superposed results are used to generate a structural model for evaluation under multiple loading conditions limits the ability to obtain quantitative performance metrics. An interesting direction for future work would be to automate the generation of stiffeners from image-based data within an FEA loop. This would enable the integration of additional mechanical constraints that are difficult to incorporate directly into the TO process, such as buckling, fatigue, and manufacturing limitations. It is also important to note that the scope of this thesis is limited, as no industrial data or constraints were available as inputs in this study.

# CHAPTER 5 CONCLUSION

## 5.1 Summary of Works

In this Master's, we explored how to interpret density-based TO results and we developed a dual performance metric that balances interpretability and structural rigidity. This approach offers a systematic methodology by assigning a score based on intrinsic mathematical data from the density-based TO, complementing the intuition and experience of structural engineers.

The process begins with defining the design space and boundary conditions. Next, we establish optimization parameters and perform a mesh refinement to ensure appropriate mesh convergence for subsequent optimizations. Once the mesh is validated, multiple optimizations are conducted, and the most effective designs are selected based on the developed performance metric. When multiple solutions appear promising, we can combine several density-based TO results to generate a more comprehensive and robust final design.

This performance metric was then applied to determine the optimal stiffening pattern for a BWB aircraft. This analysis enabled the identification of load paths under various loading conditions, including upbending, dynamic landing, roll, and engine thrust. Each stiffening pattern for all load cases was then superimposed, assuming equal weighting. Applying a binary threshold then allows to filter out the less relevant stiffening patterns. For demonstration purposes, the stiffened shell structure corresponding to the upbending load case was fabricated using 3D printing. While this process can be replicated, it falls outside the main scope of the thesis. Therefore, the methodology for extracting the TO results and generating a stiffened shell is detailed in Appendix B.

## 5.2 Achievement of Research Objectives

Three sub-objectives were defined to guide the development of the proposed methodology. SO1 aimed to develop a performance metric to evaluate TO results, taking into account both structural rigidity and interpretability. This objective was achieved and validated in Chapter 3, where the proposed metric demonstrated its ability to support the identification of the most efficient structure based on the stiffness-to-weight ratio, without relying on subjective interpretation. SO2 focused on determining the optimal stiffener layout for a BWB aircraft using TO results obtained under multiple loading scenarios. This sub-objective was successfully addressed in Chapter 4, where four load cases : upbending, landing, roll, and

engine thrust were analyzed using TO. The density-based TO performance metric was then applied to objectively select the most efficient configuration for each case, helping to identify distinct and meaningful load paths. This made it possible to merge the results from different load cases and identify recurring patterns across the complex load paths using image based post-processing. Finally, SO3 involved the development of a visual guideline for the execution of the developed framework. This was also completed in Chapter 4, where a diagram was introduced to illustrate the overall process used throughout the thesis and can be used by structural engineers in their use of TO.

## 5.3 Limitations

The developed performance metrics used for TO do not include a complexity-based score. Incorporating such a metric could be highly beneficial when comparing multiple TO results that exhibit similar performance from an interpretability and stiffness point of view, providing a more comprehensive evaluation framework.

The BWB geometry used in this study was derived from literature-based dimension ratios. However, the aerodynamic skin was not optimized to achieve the optimal lift-to-drag ratio, meaning that the resulting geometry does not precisely represent a real-world BWB aircraft. Furthermore, the multiple load cases considered in this study, while relevant, do not fully capture the actual boundary conditions of a real BWB. For the sake of simplification, these conditions were approximated, which affect the accuracy of the optimization outcomes. The pressure load case, being one of the most critical, was not considered in this study due to its complexity and the significant time required to obtain meaningful results. An important limitation is the absence of an FEA loop during the postprocessing stage, where image-based algorithms are used. Establishing a connection between the image-derived results and FEA analysis could enable further optimization and provide validation for the superimposed structure.

## 5.4 Future Research

Future research could focus on enhancing the performance metric by incorporating a complexity score into the existing evaluation framework for density-based TO. Such a refinement would enable a more holistic comparison of different TO results when adding manufacturing constraint.

Additionally, the methodology presented in this Master's could be applied to a computational fluid dynamics optimized BWB geometry that incorporates real-world system requirements

and control surfaces. More accurate load cases, reflecting the true operational conditions of a BWB aircraft, could also be integrated to improve the fidelity of the optimized topology.

Another promising avenue for future research is the incorporation of linear static analysis, modal analysis, and buckling analysis into the post-conceptual phase. These analyses would facilitate the subsequent structural sizing and validation of the optimized topology for final aircraft design.

The integration of artificial intelligence-powered design algorithms with advanced manufacturing technologies holds great promise for enhancing the structural efficiency of next-generation aircraft such as the BWB, thereby supporting the broader objective of achieving net-zero emissions in the aviation industry.

# REFERENCES


[1] P. Okonkwo and H. Smith, "Review of evolving trends in blended wing body aircraft design," *Progress in Aerospace Sciences*, vol. 82, pp. 1–23, Apr. 2016. [Online]. Available: https://www.sciencedirect.com/science/article/pii/S0376042115300336

[2] "X-48B Blended Wing Body Research Aircraft Makes First Flight - NASA," section: Armstrong Flight Research Center. [Online]. Available: https://www.nasa.gov/news-release/x-48b-blended-wing-body-research-aircraft-makes-first-flight/

[3] "X-48B Blended Wing Body - NASA," Feb. 2010, section: Aeronautics. [Online]. Available: https://www.nasa.gov/aeronautics/x-48b/

[4] "United Airlines Invests in JetZero." [Online]. Available: https://www.jetzero.aero/united-investment-announcement

[5] C. Legros, "Étude de la stabilité d'un avion BWB (Blended Wing Body) de 200 passagers," Master's thesis, École Polytechnique de Montréal, Sep. 2015. [Online]. Available: https://publications.polymtl.ca/1923/#

[6] "Our Commitment to Fly Net Zero by 2050." [Online]. Available: https://www.iata.org/en/programs/environment/flynetzero/

[7] R. Merino-Martinez, "Design and Analysis of the Control and Stability of a Blended Wing Body Aircraft," Ph.D. dissertation, Jun. 2014.

[8] "Advantages and disadvantages of BWB configuration." [Online]. Available: https://www.researchgate.net/figure/Advantages-and-disadvantages-of-BWB-configuration_tbl1_334518797

[9] M. Voskuijl, G. L. Rocca, and F. Dircken, "CONTROLLABILITY OF BLENDED WING BODY AIRCRAFT."

[10] W. Zhao and R. Kapania, "Actuator Energy and Drag Minimizations of Blended-Wing-Body with Variable Camber Continuous Trailing-edge Flaps," *Engineering Optimization*, Sep. 2019.

[11] S. Handa and G. Srinivas, "Recent developments of blended wing body aircraft: experimental, numerical and theoretical approaches," *Aerospace Systems*, vol. 5,

no. 2, pp. 171–183, Jun. 2022. [Online]. Available: https://doi.org/10.1007/s42401-022-00133-1

[12] A. Sharma, "Aerodynamic Design and Flow Separation Control Over A Blended Wing Body Transonic Aircraft Using Synthetic Jet Actuator Arrays," Ph.D. dissertation, May 2011.

[13] "22.12.2. Monocoque Type." [Online]. Available: https://www.abbottaerospace.com/aa-sb-001/22-aircraft-specific-design-features-and-design-methods/22-12-53-fuselage/22-12-2-monocoque-type/

[14] "3.3. Stiffened Shells | 3: Aerospace Structures | Introduction to Aerospace Structures and Materials | edX." [Online]. Available: https://learning.edx.org/course/course-v1:DelftX+AEASM1x+1T2024/block-v1:DelftX+AEASM1x+1T2024+type@sequential+block@de6a77a104f04af08f4a8ed95ada10a5/block-v1:DelftX+AEASM1x+1T2024+type@vertical+block@246cc2efff084a039df96d342d856aea

[15] "Material Properties | AEASM1x | edX." [Online]. Available: https://courses.edx.org/courses/course-v1:DelftX+AEASM1x+1T2024/5bf42e09c73e4801acfffe0358bac081/

[16] S. Singh and P. Pande, "Composite fuselages: How they changed the airline industry," Sep 2023. [Online]. Available: https://simpleflying.com/composite-fuselages/#:~:text=As%20we%20discussed%20in%20detail,its%20weight%20savings%20over%20aluminum.

[17] P. V. Marcal and N. Yamagata, Eds., *Design and Analysis of Reinforced Fiber Composites*, 1st ed. Cham: Springer International Publishing : Imprint: Springer, 2016.

[18] J. Hardiman, "The McDonnell Douglas Blended Wing Concept," Dec. 2021, section: History. [Online]. Available: https://simpleflying.com/the-mcdonnell-douglas-blended-wing-concept/

[19] "Gallery: Three Decades of Blended Wing Body Development | Aviation Week Network." [Online]. Available: https://aviationweek.com/gallery-three-decades-blended-wing-body-development

[20] "Table 4 : Weight analysis of a BWB-450-like aircraft with a mission of..." [Online]. Available: https://www.researchgate.net/figure/Weight-analysis-of-a-BWB-450-like-aircraft-with-a-mission-of-478-passengers-and-8-700-nm_tbl1_252069398

[21] R. H. Liebeck, "Design of the Blended Wing Body Subsonic Transport."

[22] "X-48 Research All good things must come to an end," Apr. 2013, section: Armstrong Flight Research Center. [Online]. Available: https://www.nasa.gov/centers-and-facilities/armstrong/x-48-research-all-good-things-must-come-to-an-end/

[23] "Assessment on critical technologies for conceptual design of blended-wing-body civil aircraft - ScienceDirect." [Online]. Available: https://www.sciencedirect.com/science/article/pii/S1000936119302493

[24] "Imagine travelling in this blended wing body aircraft | Airbus," Sep. 2021, section: Innovation. [Online]. Available: https://www.airbus.com/en/newsroom/stories/2020-11-imagine-travelling-in-this-blended-wing-body-aircraft

[25] "Bombardier moves to second prototype of its blended-wing Ecojet," May 2023, section: Aircraft. [Online]. Available: https://newatlas.com/aircraft/bombardier-ecojet-blended-wing/

[26] "JetZero." [Online]. Available: https://www.jetzero.aero

[27] T. Rochefort-Beaudoin *et al.*, "Supervised deep learning for the moving morphable components topology optimization framework," *Engineering Applications of Artificial Intelligence*, vol. 123, p. 106436, Aug. 2023. [Online]. Available: https://www.sciencedirect.com/science/article/pii/S0952197623006206

[28] J.-F. Gamache *et al.*, "Topology Optimization for Stiffened Panels: A Ground Structure Method." American Society of Mechanical Engineers Digital Collection, Nov. 2020. [Online]. Available: https://dx.doi.org/10.1115/DETC2020-22103

[29] M. P. Bendsøe and O. Sigmund, *Topology optimization: theory, methods, and applications*, 2nd ed., ser. Engineering online library. Berlin Heidelberg: Springer, 2004.

[30] D. Yago *et al.*, "Topology Optimization Methods for 3D Structural Problems: A Comparative Study," *Archives of Computational Methods in Engineering*, vol. 29, no. 3, pp. 1525–1567, May 2022. [Online]. Available: https://doi.org/10.1007/s11831-021-09626-2

[31] Z. Li, T.-U. Lee, and Y. M. Xie, "Interactive Structural Topology Optimization with Subjective Scoring and Drawing Systems," *Computer-Aided Design*, vol. 160, p. 103532, Jul. 2023. [Online]. Available: https://www.sciencedirect.com/science/article/pii/S0010448523000647

[32] D. Liu *et al.*, "Detailed design of a lattice composite fuselage structure by a mixed optimization method," *Engineering Optimization*, vol. 48, no. 10, pp. 1707–1720, Oct. 2016, publisher: Taylor & Francis _eprint: https://doi.org/10.1080/0305215X.2015.1125262. [Online]. Available: https://doi.org/10.1080/0305215X.2015.1125262

[33] "Topology Optimization of Fuselage - Nicolas Kawski, STELIA Aerospace." [Online]. Available: https://speakerdeck.com/altairhyperworks/topology-optimization-of-fuselage-nicolas-kawski-stelia-aerospace

[34] "STELIA Aerospace Introduces Demonstrator for 3D-Printed Aluminum Fuselage Panels," May 2018. [Online]. Available: https://www.lightmetalage.com/news/industry-news/aerospace/stelia-aerospace-introduces-demonstrator-3d-printed/

[35] N. Aage *et al.*, "Giga-voxel computational morphogenesis for structural design," *Nature*, vol. 550, no. 7674, pp. 84–86, Oct. 2017, publisher: Nature Publishing Group. [Online]. Available: https://www.nature.com/articles/nature23911

[36] J.-F. Gamache *et al.*, "Complexity-driven layout exploration for aircraft structures," *Design Science*, vol. 9, p. E13, 05 2023.

[37] "Minimum Member Size Control." [Online]. Available: https://2020.help.altair.com/2020.1/hwdesktop/altair_help/topics/solvers/os/mfg_topology_min_member_size_control_r.htm

# APPENDIX A BWB TO RESULTS

## A.1 UPBENDING TO RESULTS

Table A.1 UPBENDING TO RESULTS. XX implies that no constraint was used

| MINDIM | MAXDIM | Number of Iterations | DI [%] | Stiffness Score [%] | Overall Score [%] | Top View | Bottom View |
|---|---|---|---|---|---|---|---|
| XX | XX | 50 | 80.0 | 81.0 | 80.5 | 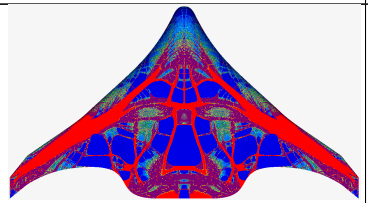 | 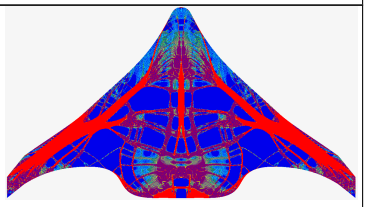 |
| 3 | XX | 97 | 96.0 | 79.7 | 87.9 | 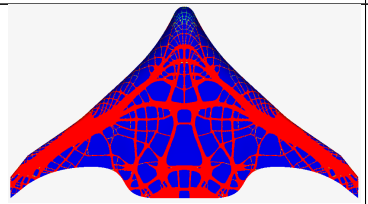 | 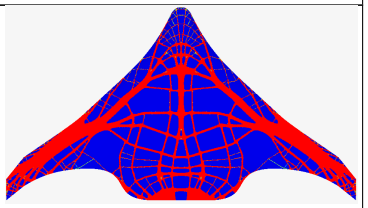 |
| 6 | XX | 106 | 96.0 | 79.4 | 87.7 | 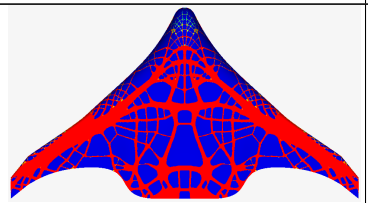 | 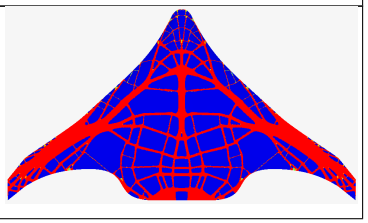 |

| MINDIM | MAXDIM | Number of Iterations | DI [%] | Stiffness Score [%] | Overall Score [%] | Top View | Bottom View |
|---|---|---|---|---|---|---|---|
| 9 | XX | 116 | 94.0 | 78.7 | 86.4 | 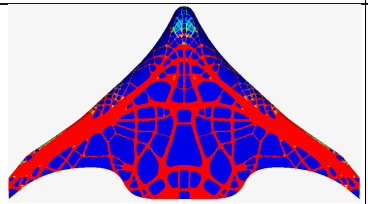 | 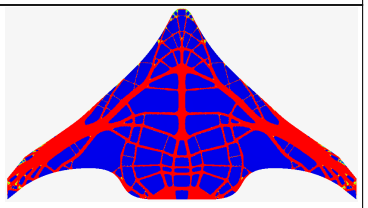 |
| 3 | 20 | 184 | 56.0 | 52.0 | 54.0 | 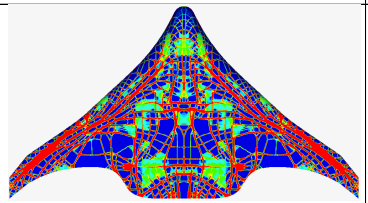 | 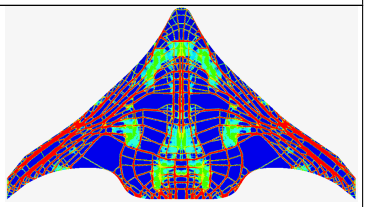 |
| 3 | 30 | 137 | 65.0 | 59.1 | 62.1 | 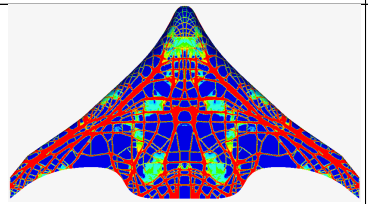 | 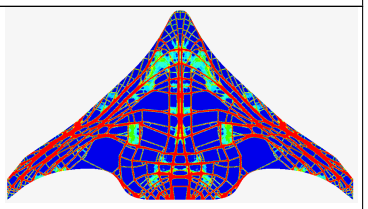 |
| 3 | 40 | 100 | 41.0 | 9.5 | 25.2 | 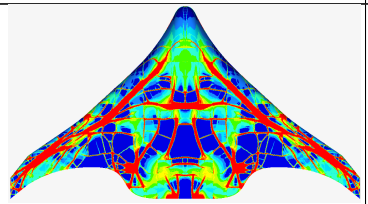 | 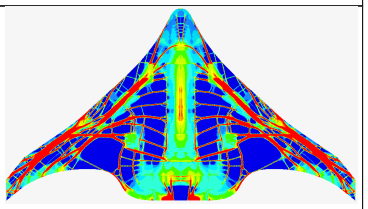 |
| 3 | 50 | 138 | 51.0 | 48.5 | 49.7 | 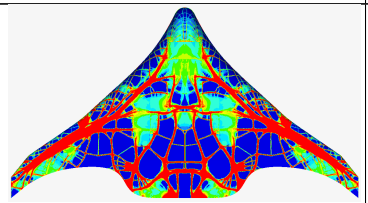 | 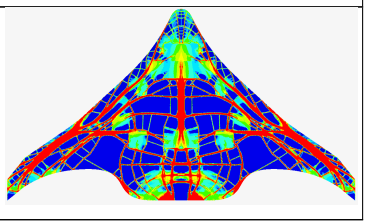 |

## A.2 LANDING TO RESULTS

Table A.2 LANDING TO RESULTS

| MINDIM | MAXDIM | Number of Iterations | DI [%] | Stiffness Score [%]* | Overall Score [%] | Top View | Bottom View |
|---|---|---|---|---|---|---|---|
| XX | XX | 38 | 82.0 | 94.6 | 88.3 | 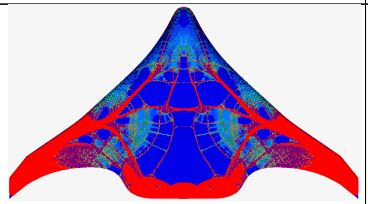 | 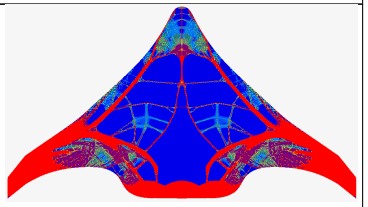 |
| 3 | XX | 84 | 96.0 | 94.5 | 95.2 | 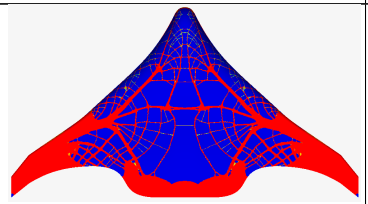 | 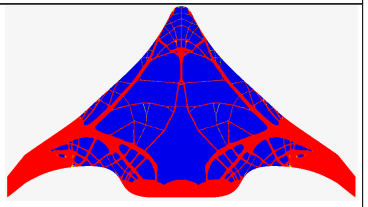 |
| 6 | XX | 85 | 96.0 | 94.3 | 95.1 | 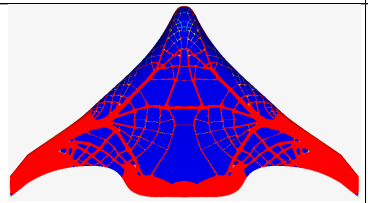 | 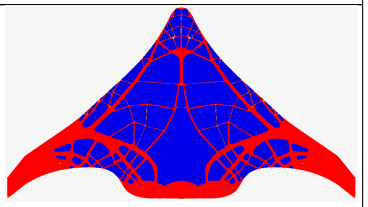 |
| 9 | XX | 85 | 95.0 | 94.0 | 94.5 | 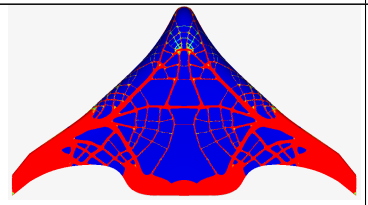 | 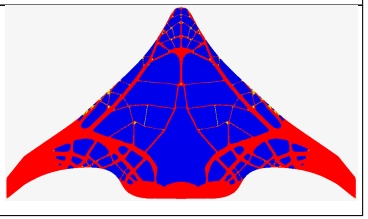 |

| MINDIM | MAXDIM | Number of Iterations | DI [%] | Stiffness Score [%]* | Overall Score [%] | Top View | Bottom View |
|---|---|---|---|---|---|---|---|
| 3 | 20 | 68 | 9.0 | 0 | 4.5 | 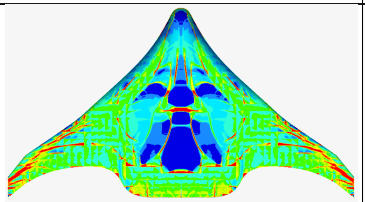 | 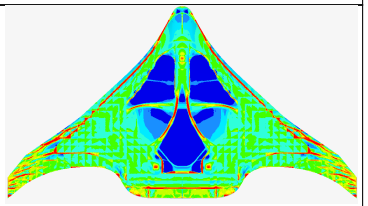 |
| 3 | 30 | 64 | 12.0 | 0 | 6.0 | 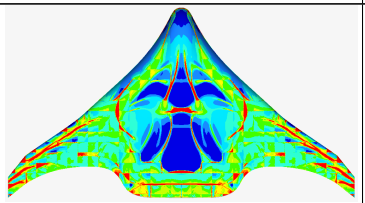 | 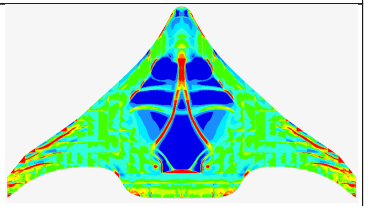 |
| 3 | 40 | 76 | 23.0 | 5.7 | 14.3 | 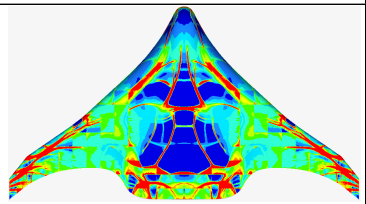 | 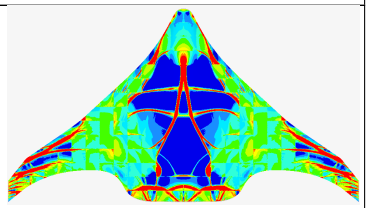 |
| 3 | 50 | 68 | 18.0 | 0 | 9.0 | 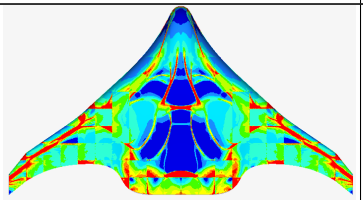 | 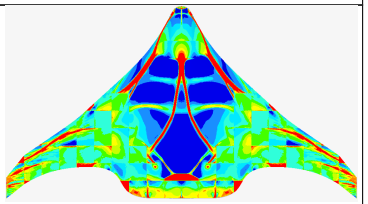 |

* Stiffness score was set to 0% if the compliance at the end of the TO is higher than the initial compliance. Generally, this means that the MAXDIM constraint can't let the optimization process converge to a local minimum.

## A.3 ROLL TO RESULTS

Table A.3 ROLL TO RESULTS

| MINDIM | MAXDIM | Number of Iterations | DI [%] | Stiffness Score [%] | Overall Score [%] | Top View | Bottom View |
|---|---|---|---|---|---|---|---|
| XX | XX | 41 | 82.0 | 96.6 | 89.3 | 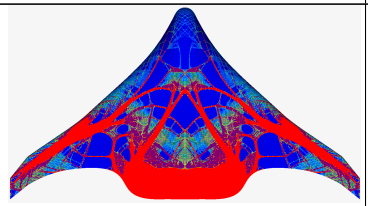 | 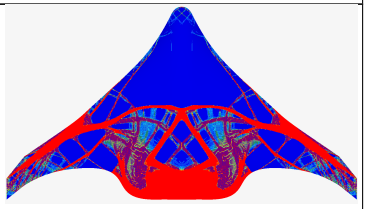 |
| 3 | XX | 74 | 95.0 | 96.4 | 95.7 | 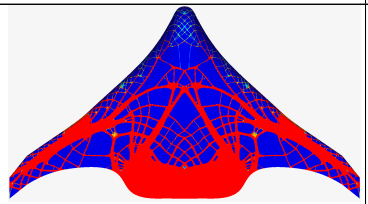 | 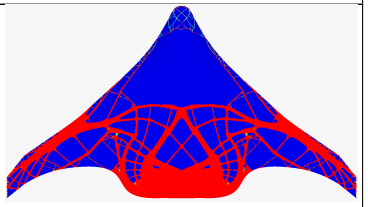 |
| 6 | XX | 76 | 94.0 | 96.3 | 95.1 | 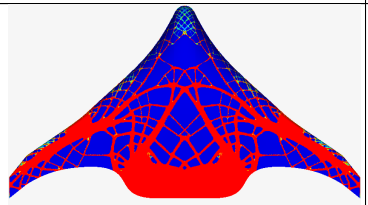 | 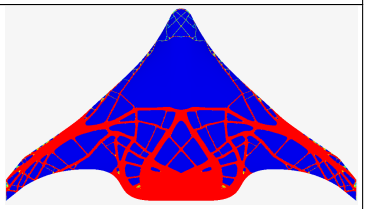 |
| 9 | XX | 72 | 92.0 | 96.0 | 94.0 | 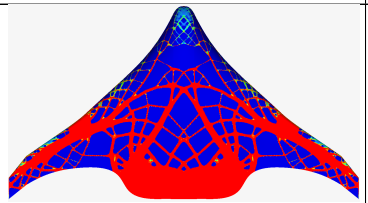 | 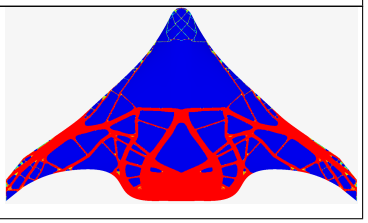 |

| MINDIM | MAXDIM | Number of Iterations | DI [%] | Stiffness Score [%] | Overall Score [%] | Top View | Bottom View |
|---|---|---|---|---|---|---|---|
| 3 | 20 | 98 | 11.0 | 37.9 | 24.5 | 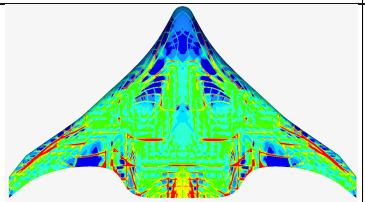 | 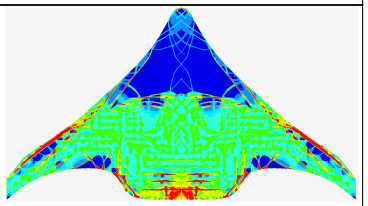 |
| 3 | 30 | 81 | 11.0 | 32.9 | 21.9 | 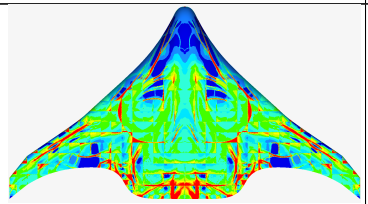 | 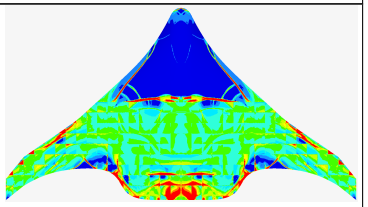 |
| 3 | 40 | 113 | 16.0 | 47.0 | 31.5 | 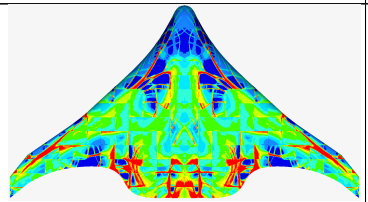 | 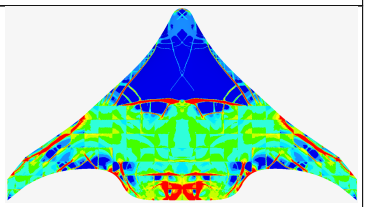 |
| 3 | 50 | 93 | 17.0 | 41.4 | 29.2 | 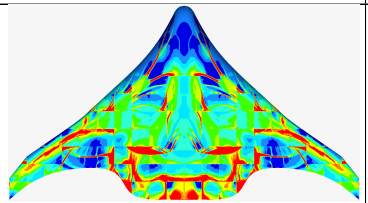 | 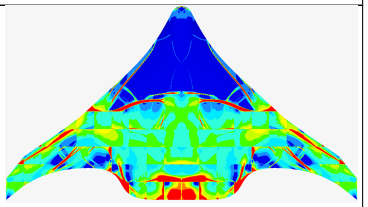 |

## A.4 ENGINE THRUST TO RESULTS

Table A.4 ENGINE TO RESULTS

| MINDIM | MAXDIM | Number of Iterations | DI [%] | Stiffness Score [%]* | Overall Score [%] | Top View | Bottom View |
|---|---|---|---|---|---|---|---|
| XX | XX | 38 | 89.0 | 87.0 | 88.0 | 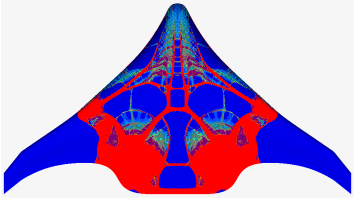 | 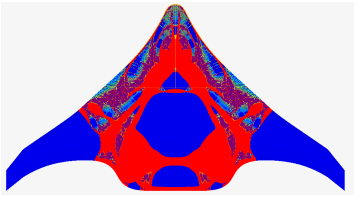 |
| 3 | XX | 67 | 97.0 | 91.5 | 94.3 | 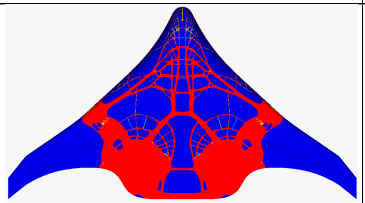 | 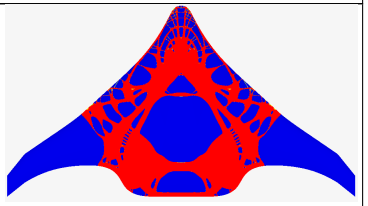 |
| 6 | XX | 62 | 97.0 | 91.4 | 94.2 | 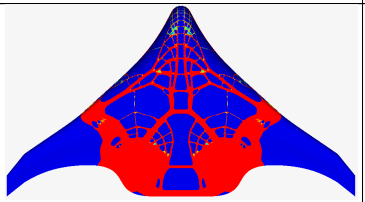 | 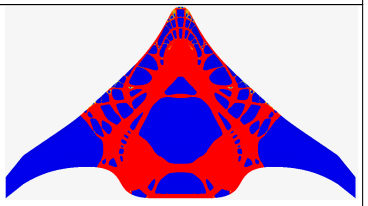 |
| 9 | XX | 67 | 95.0 | 91.3 | 93.1 | 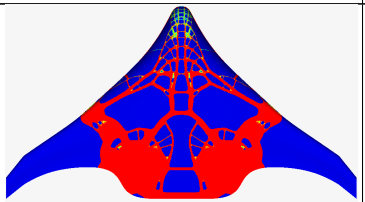 | 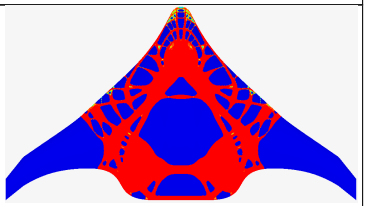 |

| MINDIM | MAXDIM | Number of Iterations | DI [%] | Stiffness Score [%]* | Overall Score [%] | Top View | Bottom View |
|---|---|---|---|---|---|---|---|
| 3 | 20 | 124 | 39.0 | 46.9 | 43.0 | 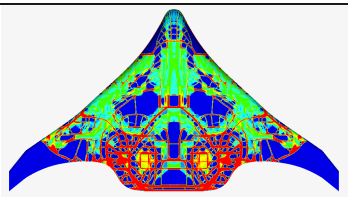 | 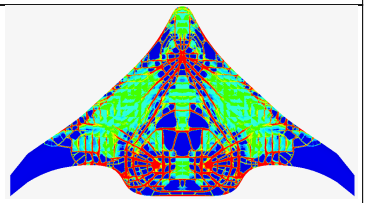 |
| 3 | 30 | 70 | 16.0 | 0 | 8.0 | 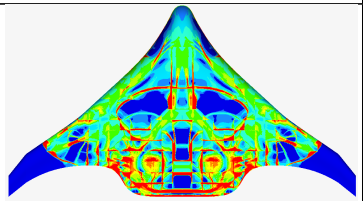 | 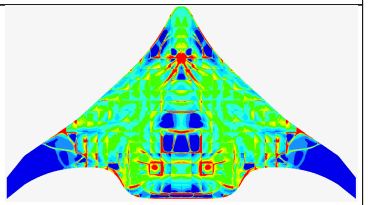 |
| 3 | 40 | 87 | 27.0 | 20.7 | 23.9 | 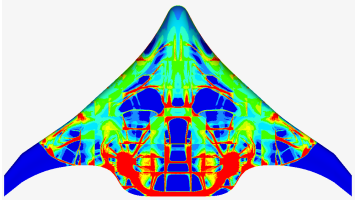 | 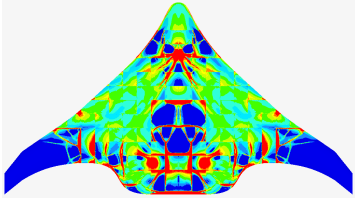 |
| 3 | 50 | 72 | 30.0 | 21.2 | 25.6 | 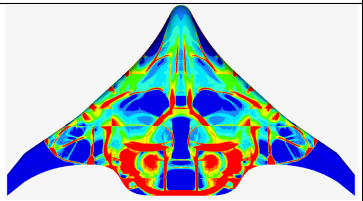 | 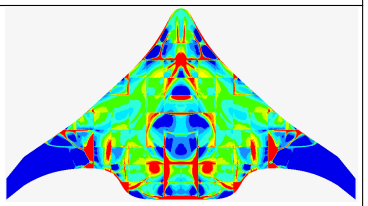 |

* Stiffness score was set to 0% if the compliance at the end of the TO is higher than the initial compliance. Generally, this means that the MAXDIM constraint can't let the optimization process converge to a local minimum.

# APPENDIX B ADDITIVE MANUFACTURING OF THE BWB MODEL STIFFENED SHELL USING TOPOLOGY OPTIMIZATION RESULTS

The model can be manufactured to demonstrate the potential of using TO combined with additive manufacturing to generate such a complex and optimized structure. For simplicity, only the optimal topology corresponding to the upbending load with the stiffened shell structure case will be fabricated. This chapter concludes the thesis by evaluating SO3, thereby demonstrating the fulfillment of the main research objective.

This methodology consists of two main steps before the additive manufacturing process: topology extraction and integration with the aerodynamic skin.

## B.1 Topology Extraction

The objective is to obtain a functional geometry from a topology optimization result. In HyperMesh, the OSSmooth tool in OptiStruct is designed to generate a refined geometry based on structural optimization outputs. This approach ensures that the extracted geometry remains free from subjective interpretation.

In this study, OSSmooth is utilized to interpret TO results and convert them into a smooth surface representation. The extracted surface is built on a triangular mesh and the structural members are identified using a density-based threshold. Although a connection detection threshold could have been considered, the high discreteness index of the TO result, approximately 96%, allows the use of a density threshold of 0.2. This ensures all structural members are included without excessive material addition. The OSSmooth tool is configured with the input parameters in Table B.1.

Table B.1 Table of the parameters for topology extraction using OSSmooth tool embedded into Altair HyperMesh

| | |
|---|---|
| **Design interpretation** | Geometry |
| **Output** | STL |
| **Geometry Options** | Load geometry |
| **Iso** | True |
| **Threshold** | 0.2 |

After extracting the surface mesh, Blender is used to introduce thickness to the mesh based geometry. The thickness is chosen based on the additive manufacturing process for the

demonstrator and is explained more in detail in Section B.2 and Section B.3. The optimized structural members are then thickened relative to the normal of the aerodynamic surface, to give results shown in Figure B.1 and Figure B.2.

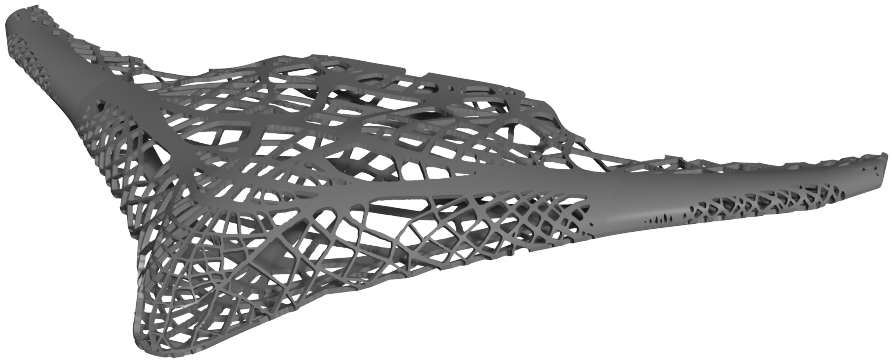

Figure B.1 Isometric view of the extracted topology for the stiffened shell BWB under the upbending load case

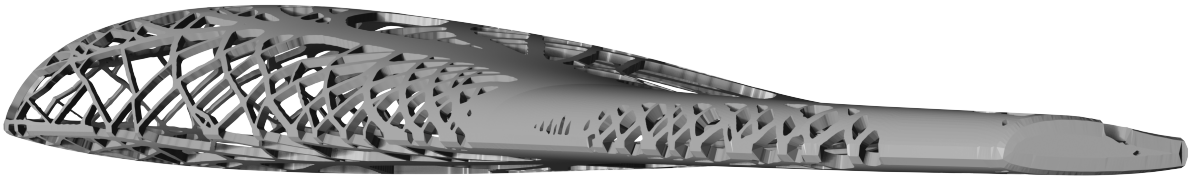

(a) Side view

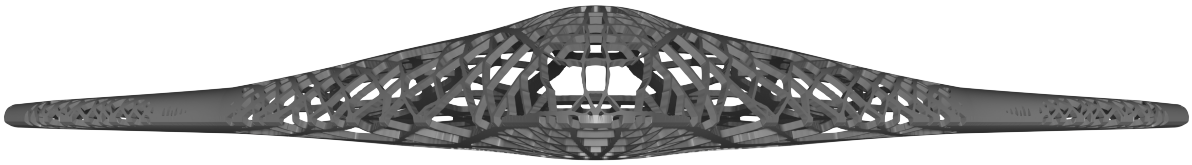

(b) Front View

Figure B.2 Side and front view of the extracted topology for the stiffened shell BWB under the upbending load case

## B.2 Computer Aided Design Integration of the Aerodynamic Skin and Topology Optimization Results

The next step involve the integration of the extruded stiffener path into the thickened aerodynamic skin. The stiffeners are two times the height of the skin as it is provides a good visual contrast. For a shell structure under real loads, a sizing optimization is necessary for commercial applications. This process results in the creation of a stiffened shell structure derived from the TO results and can be seen in Figure B.3.

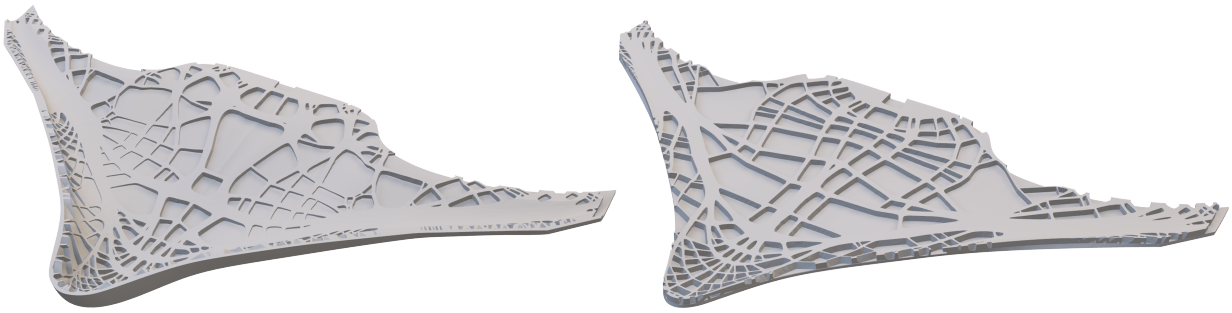

(a) Top section (b) Bottom section

Figure B.3 Internal view of the BWB stiffened shell structure optimized for the upbending load case

This methodology is based on mesh modifications and can be automated to generate complex parametric CAD models. The extracted 3D topology can then be integrated with the aerodynamic skin to form the stiffened shell structure of the BWB. However, for practical applications, a detailed sizing analysis would be required to ensure structural viability for commercial use.

## B.3 3D Printed Model of the Optimized BWB Stiffened Shell Structure

For visualization and manufacturing purposes, the top and bottom sections of the aircraft are separated to reveal the stiffener paths within the shell structure. The model is 3D printed using a standard fused deposition modeling printer with grey PLA and is divided into four parts: bottom left, bottom right, top left, and top right. The nozzle used have a diameter of 0.6mm and the skin has been modeled to have a thickness of two layer width as it is enough stiff while still being thin. Each top and bottom sections are then joined together using plastic welding to form a complete segment of the BWB. Figures B.4 shows the top and bottom sections, respectively, based on the extracted topology.

(a) Top section (b) Bottom section

Figure B.4 Internal view of the 3D printed stiffened shell BWB optimized for the upbending load case

This procedure shows how a complex double curvature panel with integrated stiffeners resulting from TO could be manufactured using advancement in additive manufacturing technology.